TMDU

TOKYO MEDICAL AND DENTAL UNIVERSITY

Morphological Assessment and Optical Characterization of Dental Hard Tissue after De- and Remineralization

Ilnaz Hariri

Morphological Assessment and Optical Characterization of Dental Hard Tissue after De- and Remineralization

Ilnaz Hariri

Promoter: Professor Junji Tagami

Cariology and Operative Dentistry

Oral Restitution Department

Graduate School Tokyo Medical and Dental University

This thesis is submitted in partial fulfillment of the requirements for the degree of *Doctor of Philosophy in Dental Science.*

Tokyo, Japan

2012

Dedication

To my late father Mohammad R Hariri, my mother Mahin Afshar, my brother Dr. Ali Hariri and most importantly my husband Dr. Darioush Alidoust, for their help and encouragement over the years.

Acknowledgments

The works presented in this thesis were carried out at Cariology and Operative Dentistry, Oral Restitution Department, Graduate School of Medical and Dental Sciences, Tokyo Medical and Dental University (TMDU) from 2008 to 2012, and were supported by the Global Center of Excellence (GCOE), International Research Center for Molecular Science in Tooth and Bone Diseases (IRCMSTBD) at our university TMDU. This thesis and the degree of PhD are the outcome of efforts and assistance by several people from different universities and organizations. I would like to express my deepest gratitude to all who contributed to this final product and to those who are not mentioned below.

Firstly, I would like to express my sincere gratitude to Professor **Junji Tagami**, Professor and Chairman of Cariology and Operative Dentistry, Oral Restitution Department, TMDU, GCOE Program, FRMDRTB at TMDU, who kindly provided me the opportunity and facilities to undertake this study, for sharing his immense knowledge of

research and life and for his always support.

My gratitude and appreciation to my supervisor, Dr. **Yasushi Shimada**, who has supported me throughout my work with his patience and knowledge whilst allowing me the room to work in my own way.

I wish to acknowledge my sincere gratitude to my other supervisor, Dr. **Alireza Sadr**, for all his generosity in teaching and his constant supportive attitude towards my work. His guidance and scientific experiences were essential for the development, process, and conclusion of the studies herein. Without him this thesis, too, would not have been completed or written.

I am deeply grateful to Dr. **Syozi Nakashima**, for his significant and critical comments on the studies presented in this thesis. His guidance, knowledge and suggestions were essential for the outcome of my research.

The academic staff of Cariology and Operative Dentistry, Oral Restitution Department, especially Dr. Masayuki Otsuki, Dr. Toru Nikaido, Dr. Masatoshi Nakajima, Dr. Yuichi Kitasako, Dr. Takako

Yoshikawa, Dr. Gou Inoue, Dr. Eitetsu Cho, Dr. Keiichi Hosaka, Dr. Tomohiro Takagaki, Dr. Naoko Seki, Dr. Rena Takahasi, Dr. Hidenori Hamba for always being friendly and for their helpful instructions and comments.

I owe my deep gratitude to Dr. Shizuko Ichinose of the Instrumental Analysis Research Center for providing useful information and to allow me to use their facilities.

My sincere thanks to my former colleagues at TMDU, for sharing unforgettable memories and helping me during my graduate studies; Dr. Shenghua Wei, Dr. Zhu Lei, Dr. Kanchana Waidyasekera, Dr. Ahmed Bakry, Dr. Na Li, Dr. Yi-Ling Tsai, Dr. Particia Makishi, Dr. Sitthikorn Kunawarote, Dr. Yuko Natsume, and to my current colleagues; Dr. Hamid Nurrohman, Dr. Amir Nazari, Dr. Prasansuttiporn Taweesak, Dr. Turki Bakhsh, Dr. Mona Mandurah, Dr. Suppason Thitthaweerat, Dr. Gerardo Mendez, Dr. Sofiqul Islam, Dr. Ena Lodha, Dr. Mohannad Nassar Michael, Dr. Ornicha Thanatvarakorn, Dr. Alaa Turkistani, and Dr. Sahar Jameel, Dr. Ehab Alsayed.

The academics and former colleagues at Dental School, Azad Tehran University.

Manufacturing companies that provided dental materials used in the experiments, especially, Kuraray Medical, Tokyo that generously supplied adhesive materials.

Lastly, I would like to thank my family for all their love and encouragement. And most of all, important thanks go to my husband, who provided the love, support, and constantly contributes to my tolerance in confronting the challenges of life. It is so wonderful to have you beside me, in the past, present, and future.

Preface

This thesis is based on the original research works by the author, to which the following articles refer.

Chapter 1. Hariri I, Shimada Y, Sadr A, Ichinose S, Tagami J. The Effects of Aging on Shear Bond Strength and Nanoleaka Expression of an Etch-and-Rinse Adhesive on Human Enamel and Dentin. *Journal of Adhesive Dentistry* 2011. [Epub ahead of print]

Chapter 2. Hariri I, Sadr A, Shimada Y, Tagami J, Sumi Y. Effects of Structural Orientation of Enamel and Dentine on Light Attenuation and Local Refractive Index: An Optical Coherence Tomography Study. *Journal of Dentistry* 2012; 40:387-396.

Chapter 3. Hariri I, Sadr A, Nakashima S, Shimada Y, Tagami J, Sumi Y. Relationship between Refractive Index and Mineral Content of Enamel and Dentin Using SS-OCT and TMR. *Lasers in Dentistry XVIII Proc. of SPIE* 2012; 8208: 82080M-1-82080M-6

Chapter 4. Hariri I, Sadr A, Nakashima S, Shimada Y, Tagami J, Sumi Y. Estimation of Enamel and Dentin Mineral Content from Refractive-Index. *Caries Research* (Submitted).

Table of Content

Introduction

Adhesive dentistry has advanced in the recent decades with the introduction of several approaches for bonding to dental hard tissues. Gaining a deeper understanding about the mechanism of adhesion to enamel and dentin leads to more favourable clinical results, increasing the durability of preventive and restorative procedures. The bond-durability, especially in dentin is strongly influenced by the stability of the components at restorative material-tooth interface, such as hybrid layer and bonding resin layer. From this point of view, evaluation of nanoleakage channel in the hybrid layer is believed to be very effective to speculate on the bond durability of the materials. In chapter 1, the nanoleakage expression and micro-shear bond strength in the etch-and-rinse resin-enamel/dentin interface has been investigated. This study attempted to determine the long-term sealing ability of etch-and-rinse adhesive system to enamel and dentin and if it was correlated to their bond strength.

Development of non-invasive medical imaging techniques has received a great amount of attention recently. A significant role among modern medical imaging techniques is played by optical methods, such as Optical coherence tomography (OCT). OCT is a non-invasive imaging technique which enables cross-sectional imaging of internal biological structures. In dental science, OCT is a useful technique for assessing early caries, oral cancer, and periodontal diseases.

In order to a deep understanding of OCT images and interpretation of the images, it is necessary to have an accurate knowledge about optical characterization of biological tissues such as teeth. Therefore, in chapter 2 optical properties of dental hard tissues such as absorption, scattering distributions and refractive index (n) and their dependence on tissue orientation relative to the irradiating light source has been investigated.

Dental hard tissues are scattering media, and their optical properties carry diagnostic information. Recent technological advances in the field of optics such as introduction of OCT have enabled accurate measurement of optical tissue properties using high-resolution imaging

devices, opening new horizons in the dental research. OCT has found a great potential in dentistry for applications ranging from caries detection to assessment of defects within dental biomaterials and tissues using cross-sectional images. One of the important parameters of light propagation in biological tissues including teeth is the *n*, which can serve as an indicator of its state and scattering properties, as scattering itself is the end result of local *n* variation. OCT has been used to investigate the *n* of sound enamel and dentin. It was suggested that early demineralization caused by caries altered *n* of enamel. Chapter 3 and 4 sought to investigate the relationship between *n* and mineral content in order to achieve alternative approaches for non-invasive early diagnosis of dental caries.

Chapter 1

The Effects of Aging on Shear Bond Strength and Nanoleakage Expression of an Etch-and-rinse Adhesive on Human Enamel and Dentin

Introduction

Adhesive dentistry has advanced in the recent decades with the introduction of several approaches for bonding to dental hard tissues. Gaining a deeper understanding about the mechanism of adhesion to enamel and dentin leads to more favorable clinical results, increasing the durability of preventive and restorative procedures. Traditionally, the adhesion to dental substrates has been achieved through the use of bonding agents that advanced micromechanical interlocking with both the enamel and dentin.(1-5) The simple acid-etching technique introduced by Buonocore(1) created microscopic roughness which increased the available surface area for bonding and made mechanical

adhesion of the penetrating resin possible. However, bonding to dentin seemed more challenging, considering its inhomogeneous nature and high organic substance. Later, bonding between resin and dentin was achieved by an acid-etching that totally removed the smear layer and demineralized dentin to facilitate the infiltration and polymerization of a hydrophilic monomer around the exposed collagen fibrils.(5, 6) Conventionally, adhesion of resin to dentin was composed of three main steps namely; etching, priming and bonding.(7, 8) In two-step etch-and-rinse adhesives, the adhesive resin is a hydrophilic mixture of the primer and bonding resin monomers, applied after rinsing the acid-etched dental substrate. In these adhesives, monomer entanglement with the collagen fibrils at the resin/dentin interface creates a mixed structure called “hybrid layer”.(9, 10) It has been suggested that the conditioned dentin surface be maintained in a moist state prior to application of the bonding resin as the acid-etched collagen undergoes shrinkage and collapse when dried. This clinical technique is commonly referred to as "wet-bonding".(11) While early *in vitro* results achieved by this approach were satisfactory with high bond strength in the laboratory tests, some

concerns were raised with regard to the long-term performance of the adhesive.(4, 12-16)

Studies on the ultrastructure of resin/dentin interface reported voids originating from spaces around collagen fibrils that were not enveloped by the infiltrating resin, and were usually located at the bottom of the hybrid layer just above the undemineralized dentin.(5, 16) The porosities and voids could create penetration paths through the network of interfibrillar spaces, which vary in size down to the nanometer range. Leakage through these pathways was termed "nanoleakage" by Sano et al.(16, 17) in contrast to microleakage, which is rather an interfacial gap between resin and dentin. Clinically, both interfacial seal and bond strength are considered to be associated with the success of a restoration.(18, 19)

To date, the majority of nanoleakage studies have focused on resin-dentin bonds, assuming that high-energy enamel surfaces created by acid-etching were optimized for resin infiltration and created a stable interface with low susceptibility to degradation over time. To the best of

our knowledge, nanoleakage expression in resin/enamel interface has not been previously studied under different thermal cycling regimens; moreover, although there are some studies which provide information on the effects of aging on both nanoleakage and bond strength of dentin, in the case of enamel, reliable data are scares.(13, 20-22) While visual assessment and scoring have been frequently used to evaluate the extent and characterize the patterns of nanoleakage expression at the interface, there is a lack of established quantitative techniques to evaluate the nanoleakage within the adhesive interface on both enamel and dentin.(15, 23, 24) Based on the above considerations, the purpose of this *in vitro* study was to perform a quantitative analysis on nanoleakage expression at adhesive interface and shear bond strength of an etch-and-rinse adhesive system under different thermal cycling regimens. The null hypotheses tested were that (1) thermocycling would not affect microshear bond strength (MSBS) of the adhesive to enamel and dentin; and that (2) thermocycling would not affect nanoleakage expression of the adhesive.

Materials and methods:

One hundred and ten freshly extracted non-carious human premolars were collected after the individual's informed consent, as approved by the Institutional Review Board of Tokyo Medical and Dental University. The teeth were stored at 4°C in saline saturated with a 0.02% thymol until use in the experiment. Eighty of the teeth were used for MSBS tests with 40 teeth for each substrate; enamel and dentin. The remaining 30 teeth were assigned for nanoleakage evaluation.

MSBS sample preparation

Two-third of the root structure was removed in all the teeth using a low-speed diamond saw (Isomet, Buehler, Lake Bluff, IL, USA) under water lubrication. Those teeth assigned to enamel groups were sectioned mesiodistally by the diamond saw to obtain two halves. On each half, the buccal or lingual enamel surface was subsequently polished with wet 600-grit silicon carbide (SiC) abrasive paper to create a flat bonding site on ground enamel (Fig. 1a). For the teeth assigned to dentin groups, slices approximately 2 mm in thickness were prepared by cutting the

tooth parallel to the mid coronal portion of the buccal surface, using the diamond saw. The samples were lightly polished on 600-grit SiC paper in order to create a standardized smear layer on the dentin surface. From each tooth two enamel or two dentin slices were obtained. The ground surface for each slice was then treated with a two-step etch-and-rinse adhesive (Adper Single Bond; 3M-ESPE, St. Paul, MN, USA) as described (Table 1).

The surfaces were conditioned with a 37% phosphoric acid gel for 15 s, and then thoroughly rinsed by water for 10 s. Acid-etched Enamel surfaces were subsequently air dried for 5 s, whereas the dentin surfaces were blotted using a cotton pellet to remove excess water, and finally left visibly moist. Two coats of the adhesive were applied to the etched surfaces using the microbrushes supplied by the manufacturer. The adhesive-coated surfaces were then gently air-dried to evaporate the solvent. Prior to light irradiation of the bonding resin on each specimen, one micro bore tygon tubing (Norton Performance Plastic; Akron, OH, USA) with an internal diameter and height of 0.75 mm and

0.5 mm respectively was placed on the enamel and dentin in each slice. The bonding resin was then irradiated for 10 s, and a universal resin composite, Clearfil AP-X shade A2 (Kuraray Medical; Tokyo, Japan) was carefully inserted into the tygon tubing and irradiated for 40 s. The specimens were stored at room temperature (23°C) for one hour after which the tygon tubing was carefully removed using a sharp blade. In this manner, very small cylinders of resin, approximately 0.75 mm in diameter and 0.5 mm in height, were bonded to the surface. The bonded specimens were then stored for 24 h in 37°C distilled water, and randomly distributed among five thermocycling groups, with 16 slices per each group as follows; group 1 was subjected to MSBS test without thermocycling (control group), groups 2, 3, 4 and 5 were thermocycled for 100, 500, 2,000 and 10,000 times respectively, and then subjected to MSBS test. For thermal cycling, the specimens were placed in a wire-mesh basket, and alternated between 5°C and 55°C water baths (Cool line CL 200 and Cool Mate TE200 apparatus Yamato Scientific; Tokyo, Japan). The dwell time was 30 s in each bath with a transfer time of 5 s. Each tooth slice with the resin cylinder was attached to the testing

device (EZ-test-500N; Shimadzu, Kyoto, Japan) with a cyanoacrylate adhesive (Zapit, Dental Ventures of America; Corona, CA, USA), and subjected to MSBS test using the wire-loop technique at a cross-head speed of 1.0 mm/min as previously described (Fig.1a).(25)

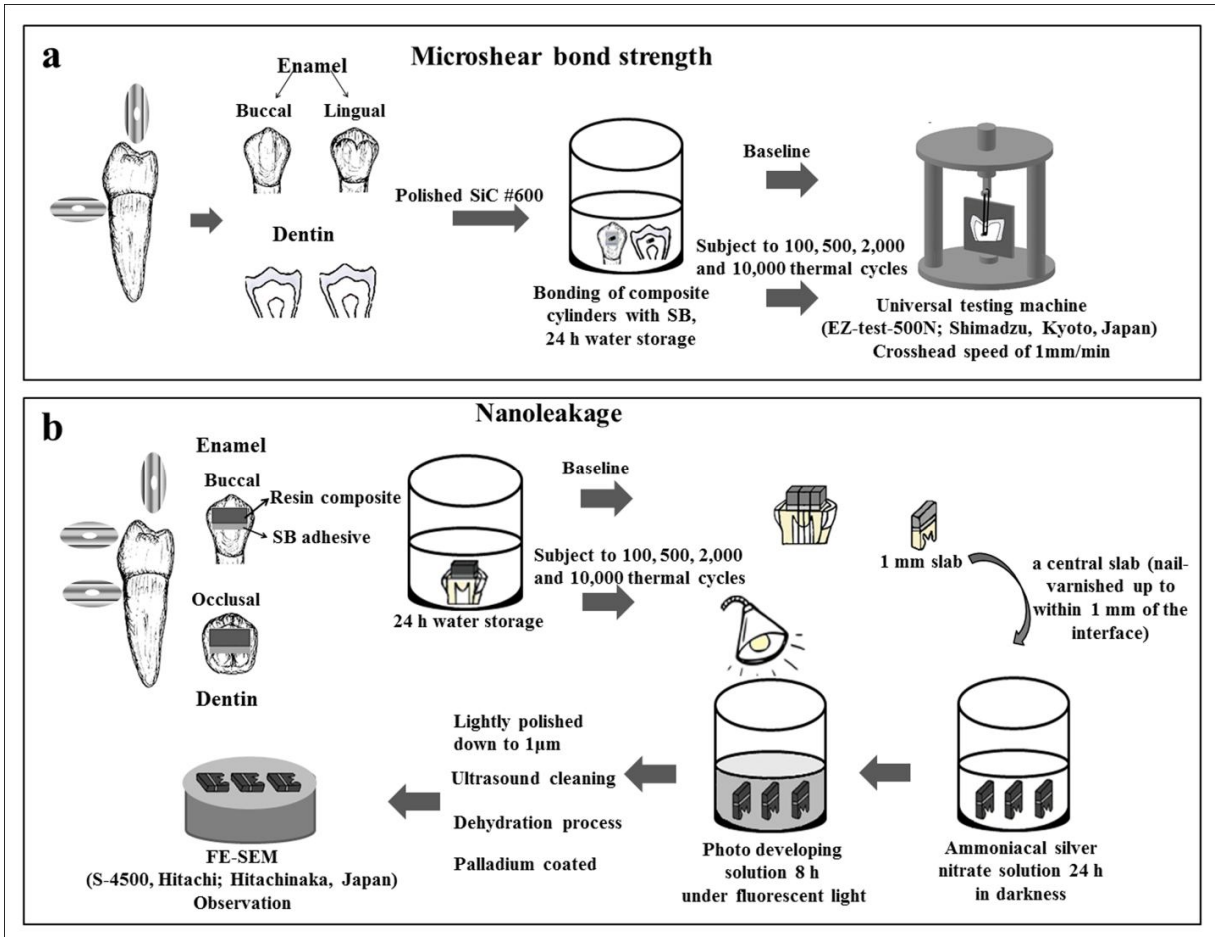

Figure 1(a) Schematic illustration of human premolar enamel and dentin prepared for MSBS test (b) Experimental design for nanoleakage evaluation.

Table 1. Materials used in this study.

Material (Manufacturer)	Lot #	Contents
Adper™SingleBond (3M ESPE)	8KY	Etchant:35% phosphoric acid Adhesive: HEMA, polyalkenoic acid copolymer, Bis-GMA, photoinitiator system, water and ethanol
Clearfil AP-X (Kuraray Medical)	01028 A	Resin Matrix: Bis-GMA, UDMA, TEGDMA Filler content (wt%): 89%
HEMA= 2-hydroxyethylmethacrylate; Bis-GMA= bis phenol A glycerolate dimethacrylate; UDMA= urethane dimethacrylate; TEGDMA; triethylene glycol dimethacrylate.		

Nanoleakage sample preparation

Buccal enamel surfaces on 15 teeth were ground (600-grit SiC paper under running water) to create flat surface on ground enamel. T expose the dentin substrate, the occlusal thirds of the remaining 15 teeth were removed by sectioning the crown at right angles to the long axis of the teeth, and the occlusal superficial dentin surface, without any enamel remnants, was finished with the 600-grit SiC paper under running water to create a standardized smear layer. The adhesive was applied to the treated surface following the same procedure for MSBS test. Clearfil AP-X was applied in two layers to create an approximately 4 mm-high composite buildup on the treated surface. Each increment was

individually light-activated for 40 s. After storage in 37°C water for 24 h, samples were distributed into the five treatment groups of 3 specimens each, and thermal stressed in the same manner as for the MSBS test.

The bonded specimens were then vertically sectioned with the diamond saw under water lubrication, through the composite buildups and the bonded tooth into approximately 1 mm-thick slabs. One central slab was chosen from each tooth, forming a total of 3 slabs per group.

The bonded slabs (enamel and dentin) were ground and polished in turn using wet SiC papers (600, 800, 1,200, 1,500, 2,000) and diamond pastes with particle sizes of (6 μm, 3 μm, 1 μm), and then coated with two layers of fast-drying nail varnish applied up to within 1 mm of the bonded interfaces. To keep the specimens hydrated, they were immersed in distilled water for 10 min prior to immersion in a tracer solution, ammoniacal silver nitrate, which was prepared according to the protocol previously described by Tay et al.(26) The slabs were placed in the ammoniacal silver nitrate in total darkness for 18 h, rinsed thoroughly in distilled water and immersed in photo developing solution for 6 h under

a fluorescent light to reduce the penetrated silver ions into metallic silver grains within voids along the bonded interface. The silver-stained resin-bonded specimens were gently polished with diamond pastes with a particle size of 1 μm and sonicated for 5 min to remove the superficial silver adsorption. The specimens were coated with a thin layer of palladium and observed using a FE-SEM (S-4500, Hitachi; Hitachinaka, Japan) (Fig. 1b).

Nanoleakage image analysis

Four locations were arbitrarily imaged at a magnification of 1500X along the interface on each slab; in total, 12 images were obtained from three teeth in each group. Each image included 77 μm length of the interface, at a resolution of 1208 pixels by 1000 pixels.

The Percent distribution of metallic silver particles at the resin-enamel and resin-dentin interfaces were calculated on the images obtained in the interfacial zone using digital image analysis software (ImageJ 1.42q, Wayne Rasband, National Institutes of Health; Bethesda, MD, USA), according to the following procedures: on enamel, the interfacial zone

included resin/enamel interface and adhesive layer. On dentin, the zone included the adhesive body and the hybrid layer. The image was trimmed to the selected interfacial zone, and a noise reducing median filter was applied to the 8-bit image. The image was then converted to a binary image using the Otsu method to distinguish the silver area (black target pixels) from the resin and tooth (white background pixels). Finally, the silver penetration on the interfacial zone was calculated in percentage by dividing the black area over the total area of the selected zone.

Statistical analysis:

In order to detect significant differences in bond-strength after each thermocycling period compared to the control, the MSBS data from each substrate were then separately analyzed using one-way ANOVAs followed by Tukey's HSD post-hoc test for multiple comparisons at a significance level of $\alpha=0.05$ ($n=16$). Two-way ANOVA was not performed due to violation of the equal variance assumption. For each group, Weibull distribution parameters were also determined using the

linear regression method at 95% confidence level as previously described.(27) Nanoleakage results in percent were analyzed by one-way ANOVA and Tukey's HSD post-hoc test when normally distributed (enamel), or otherwise by non-parametric Kruskal-Wallis and Mann-Whitney tests with Bonferroni correction (dentin), to determine groups with significantly different silver penetration compared to each other (α=0.05).

Results:

The results of MSBS test and silver penetration for enamel and dentin groups are given in Table 2. One-way ANOVA showed no statistically significant difference in enamel bond strength among groups ($p>0.05$). In dentin, there was a significant difference between groups ($p<0.05$); Tukey's HSD post-hoc test found that the bond strength was significantly lower in groups 4 and 5 compared to group 1 ($p<0.05$). Table 3 summarizes Weibull modulus (m) and 95% confidence interval (CI) of m, characteristic strength ($\sigma 0$) and 95% confidence interval (CI) of $\sigma 0$, 5% probability of failure ($\sigma 0.05$), and Weibull coefficient of

correlation (r) for each of the 10 experimental groups. The fit of experimental data with Weibull distributions (Fig. 2 a, b) was acceptable, as shown by high correlation coefficient values ($r>0.93$ in all cases). Weibull analysis indicated that the characteristic strength decreased gradually with aging in both substrates. A drop was also observed for $\sigma 0.05$, when comparing group 5 to the control in both enamel and dentin.

Figures 3 and 4 depict representative FE-SEM micrographs of resin/dentin interfaces after silver penetration, corresponding trimmed images on which the total percent distribution of silver within the defined zone was calculated, and the resulting binary. In enamel, nanoleakage occurred mainly within the adhesive layer in all groups, with spotted silver grains at the control and increased silver deposition in groups 4 and 5. On the other hand, in dentin, all groups showed silver penetration within both the adhesive and the hybrid layer. Distinct silver deposits were observed along the base of hybrid layer in group 3, and also within the entire hybrid layer thickness at some areas. In dentin groups 4 and 5, the silver penetration reached the adhesive

resin/composite interface, with remarkable nanoleakage throughout the entire thickness of the hybrid layer (Figs. 4b, c).

One-way ANOVA and Tukey's HSD post-hoc test indicated that enamel thermocycled enamel groups 2 to 5 presented a significantly higher nanoleakage percentage compared to control ($p < 0.05$). Similarly, in dentin, the non-parametric analysis indicated that groups 2 through to 5 showed significantly higher leakage when compared to control ($p < 0.05$).

Table 2. MSBS and silver penetration for all enamel groups.

		Thermal cycling group				
		(1) Baseline	**(2) 100**	**(3) 500**	**(4) 2,000**	**(5) 10,000**
MSBS MPa ±SD	ENAMEL	**41.1 ± 10.1**	**41.4 ± 13.1**	**37.3 ± 11.1**	**37.4 ± 10.4**	**34.6 ± 10.6**
Silver Penetration % ±SD	ENAMEL	**5.9±1.3^{a}**	**10.6 ± 4.5^{b}**	**11.2 ±3.5^{b}**	**13.2 ±2.9^{b}**	**18.2 ± 7.2^{c}**
MSBS MPa ±SD	DENTIN	**43. 1± 7.4^{a}**	**43.4 ± 8.4 ^{a}**	**39.1 ± 9.4 ^{a,b}**	**33.8 ± 5.9^{b}**	**31.9 ± 5.4^{b}**
Silver Penetration % ±SD	DENTIN	**3.8±3.4^{a}**	**12.5 ± 2.5^{b}**	**28.4 ±12.0^{c}**	**29.0 ±17.6 ^{c}**	**29.3 ± 6.6 ^{c}**

-Values marked by different uppercase superscript letters are significantly different. (p<0.05, Tueky HSD post hoc)
-Values marked by different uppercase superscript letters are significantly different. (p<0.05, Mann Whitney U pairwise comparison)

Table 3. Weibull modulus (m) and 95% confidence interval (CI) of m, characteristic strength (σ0) and 95% confidence interval (CI) of σ0, 5% probability of failure of σ0.05, and Weibull coefficient of correlation(r).

Thermal cycling group		*m*	*m 95% CI*	σ_0*(MPa)*	σ_0 *95% CI*	$\sigma_{0.05}$*(MPa)*	*r*
ENAMEL	(1) control	4.04	3.42-4.66	45.27	38.5-54.93	21.70	0.97
	(2) 100	3.58	3.14-4.02	45.67	38.84-55.42	19.92	0.98
	(3) 500	3.45	3.01-3.88	41.38	35.19-50.21	17.47	0.98
	(4) 2,000	3.80	3.31-4.29	41.22	35.05-50.1	18.85	0.98
	(5) 10,000	3.63	2.83-4.43	38.25	32.53-46.41	16.86	0.93
DENTIN	(1) control	6.27	5.43-7.11	46.16	39.25-56.01	28.75	0.97
	(2) 100	5.89	5.30-6.49	46.6	39.63-56.55	28.15	0.98
	(3) 500	4.91	4.19-5.65	42.43	36.09-51.49	23.20	0.97
	(4) 2,000	6.74	5.79-7.70	36.03	36.64-43.72	23.20	0.97
	(5) 10,000	6.96	5.85-8.06	33.93	28.85-41.17	22.14	0.96

Discussion:

Our aim in the current study was to investigate by aging-induced changes in bonding of an eth-and-rinse adhesive to tooth. Specimens were subjected to thermal aging ranging from 100 to 10,000 cycles. According to the ISO TR 11405,(28) 500 thermocycles in water at temperatures between 5°C and 55°C is considered to be an appropriate test for aging dental materials. In addition, 10,000 thermal cycles was suggested to correspond to approximately 1 year of *in vivo* functioning. (29)

Bond strength to both enamel and dentin generally gradually decreased with an increased number of thermal cycles; however, separate post-hoc analysis of the mean values within each substrate showed no significant differences in MSBS in enamel, while in dentin, a significant decrease was detected at 2,000 and 10,000 thermal cycles. In order to further investigate bond strength reliability, Weibull analysis was performed in this study. Weibull analysis can provide information about the reliability of an adhesive material, rather than solely relying on the mean bond strength and standard deviations.(2) Weibull modulus (m) values were in the range of values previously reported for adhesive materials bonded to teeth(30). These values were generally higher in dentin than in enamel in this study, suggesting a higher scatter in enamel bond strength results. This was in line with a previous study on MSBS of Single Bond to enamel and dentin.(31) Some authors have attributed the low Weibull modulus to the limitations of a bond test prone to high scatter from non-uniform stress states,(32) as well as a various flaws that affect strength in the specimen.(2, 33)

As seen in Figs 2a and 2b, the Weibull failure probability curves shift to the left for both substrates with increased thermal aging over 500 cycles, indicating an increased probability of failure at lower stresses; after 10,000 thermal cycles, Weibull statistics showed a decrease in characteristic strength of both enamel (15.5%) and dentin (26.5%) compared to the control. The force required to cause 5% bond failure is the type of information that has the most clinical relevance. Interestingly, the stress at the 5% failure probability in both substrates showed a substantial and similar decrease with 22.3% drop in enamel and 22.9% in dentin, compared to the control. This finding revealed that bonding to enamel was also subject to deterioration by thermal aging.

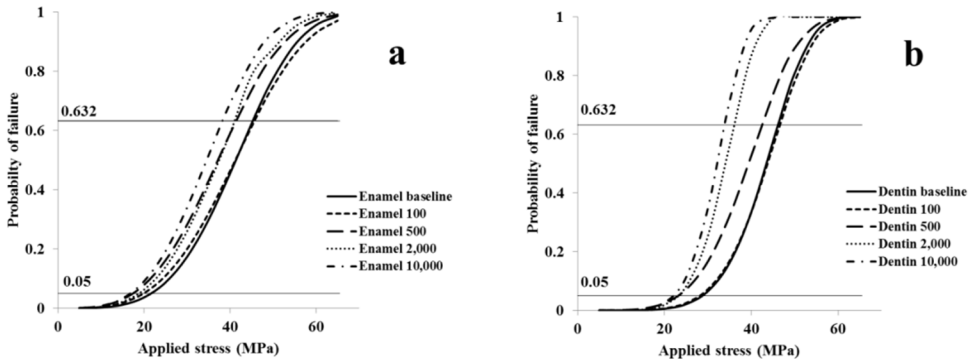

Figure 2 (a) Probability of failure vs. the stress for enamel groups (I) to (V). The lines are drawn at 63.2% and 5% probability of failure. Figure 2 (b) Probability of failure vs. the stress for dentin groups (I) to (V). The lines are drawn at 63.2% and 5% probability of failure

The findings on effects of thermocycling on bond strength of the etch-and-rinse adhesive in the current study agreed with those reported by Miyazaki et al.(14, 34) who found a small but statistically not significant decrease in the mean enamel bond strength after thermocycling, while dentin bond strengths of two-step etch-and-rinse adhesive systems significantly decreased after 30,000 thermal cycles. In another study,(35) thermocycling significantly reduced the bond strengths of the etch-and-rinse adhesive systems to bovine dentin.

The current study also examined the micro morphological appearance and interfacial nanoleakage. The aim of nanoleakage evaluation was to gain a better understanding of the mechanisms of changes exerted on the bonded complex by the thermocycling, and of the location where degradation of the bond had initiated. Visual assessment has been traditionally used to evaluate the extent of nanoleakage; however, there are only a few reports introducing different scoring methods in the literature.(22, 26, 36) In order to provide a quantitative and objective method to evaluate the extent of nanoleakage within the interfacial zone,

this study used digital imaging software (Image J 1.42q). The percentage of metallic silver particles within a selected area was calculated based on the brightness of each pixel on the digital image. Using a similar nanoleakage scoring method as in the current study, Makishi et al.(36) evaluated the percentage of silver particles within the interface resin cement/dentin interfacial zone. We included the whole bonding layer thickness (13.2 ± 5.1 μm) for percentage calculations to enable an objective analysis of the silver uptake, not only at the very interface but also throughout the adhesive body. In dentin, resin tags and hybrid layer (approximately 2 μm) were also included in the analysis. This gave consistent results in enamel with a normal distribution in groups. On dentin, however, there was a greater variability in results, requiring a nonparametric statistical analysis.

A control nanoleakage pattern in the form of thin and incontinuous silver deposition could be observed within the adhesive layer on enamel. Several mechanisms have been suggested for such leakage within adhesive layers; the silver deposits within the body of adhesive may also represent solvent-filled spaces that were not completely removed from

the adhesive prior to polymerization.(37) Even though we dried enamel surface prior to bonding, the control nanoleakage may also be due to the extremely hydrophilic nature of the primer/bonding mixture. The hydrophilic components (e.g. polyalkenoic acid copolymer) have an affinity for water via hydrogen bonding; water might be absorbed, interacting with the carbonyl groups and forming tight hydrogen bonds. The amount of water inside the polymer bulk tends to increase with time, forming large pores (water droplets) within the adhesive layer that can be stained by silver;(4, 14, 15, 23, 38, 39) this can explain the rapid progression of nanoleakage within the adhesive layer, with a significant increase observed as early as 100 thermal cycles.

Moreover, it is possible that the nanoleakage pathways were enlarged by leaching hydrophilic resin components from the polymerized resin matrices during thermal cycling. A gradual extension of nanoleakage defects within the adhesive can be explained also by the thermal fatigue, resulting in progression of defects within the structure,

Figure 3. Representative SEM micrographs obtained from silver impregnated sections of resin-enamel interfaces of bonded specimens in groups 1, 2 and 5 with the corresponding images trimmed to the interfacial zone, and their binary images obtained by digital image analysis software (Image J 1.42q) (R = Resin composite, E = Enamel, AL = Adhesive layer). (a) Resin-enamel interface in group 1. A baseline nanoleakage pattern in the form of thin and interrupted silver deposition could be observed within the adhesive layer (white arrow) phosphoric acid etching depth (white pointer).(a')Image in (a) trimmed to the selected interfacial zone. (a") Binary image of (a'). (b) The resin-dentin interface of group 4; spotted and sparse silver infiltration was detected along the resin-enamel interface (black pointer). (c) Group 5 also showed dense deposition of silver particles along the adhesive layer (arrowhead). (b') and(c')Trimmed images to the selected interfacial zone of (b) and (c). (b") and (c") Binary images of (b') and (c').

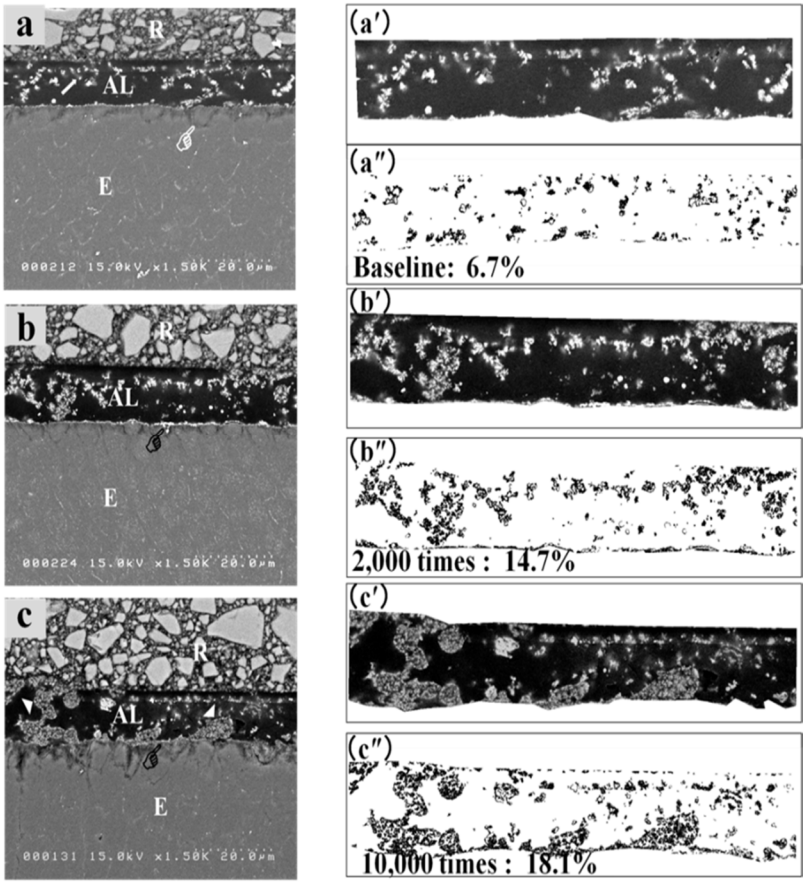

Figure 4. The resin-dentin interfaces of specimens of SB in groups 1, 4 and 5 with the corresponding images trimmed to the interfacial zone, and their binary images obtained by digital image analysis software (Image J 1.42q) (R = Resin composite, D = Dentin, AL = Adhesive layer). (a) Resin-dentin interface in group 1. Sparse silver particles were observed in the adhesive- hybrid layer interface (white arrows) and within the hybrid layer (between arrows) after 24 h (control). (a') Image in (a) trimmed to the selected interfacial zone. (a") Binary image of (a'). (b) and (c) the resin-dentin interface of groups 4 and 5 showing extensive silver deposition throughout the entire hybrid layer thickness (between arrows). The silver deposition progressed from the adhesive-hybrid layer interface toward the composite layer interface after subjecting to thermal cycling (white arrowheads). Group 4 shows great nanoleakage (black pointer) throughout the entire thickness of the hybrid layer revealing intense collagen destruction. (b') and (c') Trimmed images to the selected interfacial zone of (b) and (c). (b") and (c")Binary images of (b') and(c').

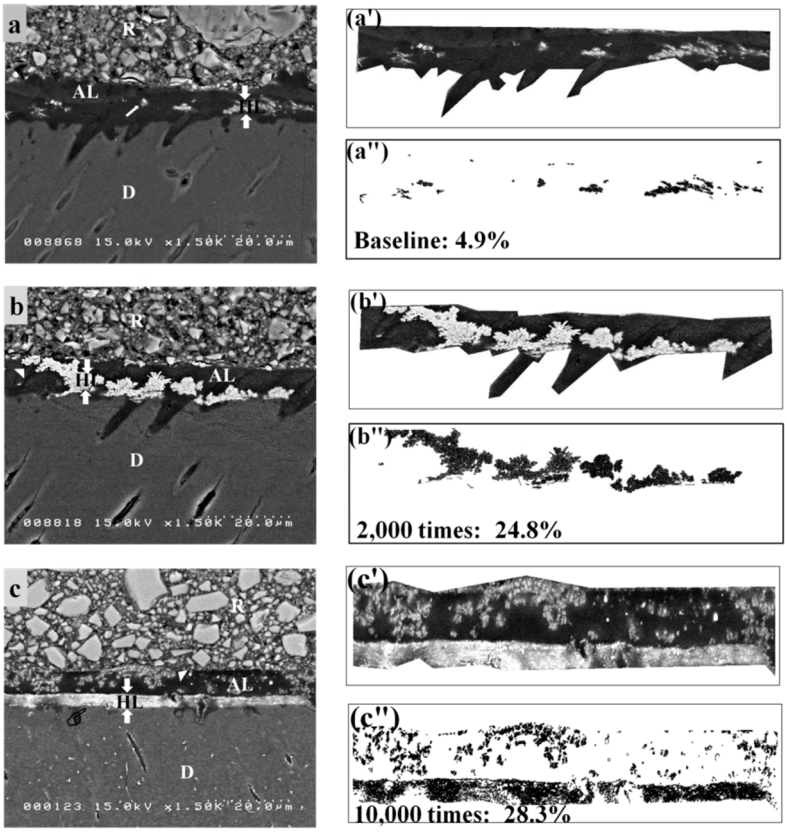

which will eventually lead to a failure. Furthermore, at the latter two aging stages in groups 4 and 5, spotted and sparse silver infiltrations were detected along the resin-enamel interface. Such interfacial silver penetration may suggest a possibility of over etching and incomplete resin infiltration at the base of phosphoric-acid-etched enamel and incomplete encapsulation of the remaining partially dissolved apatite

crystallites by the adhesive resin, more over increased thermocycling regimens may have increased water sorption and also increase the leaching of resin components.(40, 41)

While the patterns of nanoleakage within the bonding layer were similar between dentin and enamel at the control, additional long-term deterioration mechanisms were suggested for dentin. Similar to enamel, the nanoleakage of dentin groups significantly increased after only 100 thermal cycles, but with a remarkable staining of the hybrid layer. It has been reported that a discrepancy between the depth of resin penetration and dentin demineralization or poor polymerization of adhesive resin may account for the high degree of nanoleakage found at the bottom of the hybrid layer in Single Bond.(15, 21) More recently, some studies have found another kind of bond degradation at resin/dentin interface; exposed collagen fibrils might be degraded by matrix metalloproteinases (MMPs) in saliva or those slowly released from underlying mineralised matrix during aging.(12, 42) Group 5, with 10,000 thermal cycles, showed nanoleakage throughout the entire thickness of the hybrid layer

revealing intense collagen destruction. Another noteworthy finding is that the most rapid changes in nanoleakage occurred within the first 500 cycles after which, the mean nanoleakage value remained stable at around 29%, while the bond strength continued to drop. Nevertheless, the nanoleakage within enamel bond tended to continue growing up to the final stage in this study, but remained lower than that in dentin. While the correlation between the nanoleakage and clinical durability of adhesive restorations merits further study, it appeared that in comparison to the bond strength test, the nanoleakage technique could detect deterioration of the adhesion in an earlier stage. Clinically, leakage may affect durability of composite restorations, as it may serve as an initial stage towards problems ranging from margin discolouration to secondary caries or catastrophic failure.(43)

Conclusion

According to the bond strength results, the first null hypothesis was rejected, as the bond strength significantly decreased with aging in dentin. The results of nanoleakage evaluation implied that the second

hypothesis had to be rejected as well. A nanoleakage increase was detected in an earlier stage than when a significant drop was observed in bond strength, with the dentin bond being more susceptible to deterioration.

Acknowledgement

This work was supported by the Global Center of Excellence (GCOE) Program, International Research Center for Molecular Science in Tooth and Bone Diseases at Tokyo Medical and Dental University and by a Grant-in Aid from the Japan Society for the Promotion of Science (JSPS No. 19209059). Authors are grateful to Prof. Timothy J. Wright for his help in preparing the manuscript.

Chapter 2

Effects of structural orientation of enamel and dentine on light attenuation and local refractive index: An optical coherence tomography study

Introduction

Development of non-invasive medical imaging techniques has received a great amount of attention recently. Wherever possible, an attempt is made to abolish and replace invasive methods in favour of others that provide similar results without having a negative impact on the patient. A significant role among modern medical imaging techniques is played by optical methods, including scanning laser microscopy, endoscopy, fluorescent microscopy, and more recently optical tomography. (44) It has been indicated that the optical properties of human tissue may carry diagnostic significance.(44, 45)

Optical coherence tomography (OCT) is a rapidly growing non-invasive imaging technique which enables cross-sectional imaging of

internal biological structures by differentiating between scattered and transmitted or reflected photons using broad-band, near-infrared (near-IR) light sources on micron-scale resolution.(46-49) OCT was first proposed for use as a biological imaging system in 1991, (48) and has been well-established and widely developed in the field of medicine. In dentistry, the first applications were reported in the late 1990s (50) for *in vitro* and *in vivo* imaging of dental structure, and characterization of healthy teeth and caries lesions, indicating its potential in dental diagnosis.(47-49) Swept-source OCT (SS-OCT) is an implementation of the spectral discrimination OCT which time encodes spectral information by sweeping a narrow line width laser through a broad optical bandwidth. The focused light beam is projected onto the selected locations and scanned along an area of interest on the surface. Backscattered light from within the subject is coupled back with the reflected light from the reference mirror to the system by an optic fiber; the interference signal is then picked up by the light detector, digitized on a time scale and analyzed in the Fourier domain to reveal the depth information of the sample, which can be used to reconstruct cross-

sectional Images.(51) The technology has recently been widely used as an experimental method for studying dental structures and diagnosis of dental disease, including caries.(52-56)

For a deep understanding of OCT images and interpretation of images, it is necessary to understand inherent optical properties of dental hard tissues. Dental enamel comprises almost entirely of arranged arrays and densely packed hydroxyapatitie (HAp) crystals which are organized into rods called enamel prisms.(57) Enamel prisms are consistently parallel to the long axis of the tooth. The prisms are perpendicular to the surface at the edge of the cusps and occasionally at the cervical area.(58) Longitudinal light microscopic observations of ground sections of enamel reveal that the arrangement of the enamel prisms gives rise to a light and dark pattern termed Hunter–Schreger bands (HSBs). HSB is an optical phenomenon caused by the interaction of incident light and the alternating direction of adjacent groups of enamel prisms as they pass through the body of enamel from the dentine-enamel junction (DEJ) to

the external enamel surface. The appearance is most likely caused by reflection of light by prism sheaths and interprismatic material.(59-61)

On the other hand, the underlying dentine can be described as a complex structure of organic components (30 vol.%), mostly collagen fibrils, inorganic components (50 vol.%) incorporated into HAp crystals, and water (20 vol.%). The main dentine structural components are dentinal tubules, which are oriented with an S-shaped curve from the pulp cavity towards the periphery.(62, 63)

Owing to the complex and anisotropic nature of biological tissues, optical properties such as absorption and scattering distributions generally depend on tissue orientation relative to the irradiating light source.(64) Previous study has shown that enamel HAp crystals are the main components responsible for the scattering process in enamel.(65, 66) In dentine, the tubules are the most important scatterers, while the collagen fibrils and the mineral crystals play a smaller role. (63) The orientation and density of dentinal tubules may affect light scattering

through dentine, while in enamel, light scattering is relatively more isotropic.(63, 64)

n is an important parameter of light propagation in biological tissues including teeth; indeed, scattering is the end result of local *n* variation.(67) OCT is based on low-coherence interferometry and thus, can be used to measure the optical path length (OPL).(68) Since the optical thickness is the product of the *n* and the geometric thickness, OCT can provide accurate measurements of the *n* provided the geometric thickness is known.(69) Quantitative determination of n of human tissue using OCT is a simple method that can provide information on tissue structure in health and potentially carry a diagnostic value.(70) In addition, knowledge of *n* is necessary for accurate depth measurements in tissues.

In addition to optical thickness or OPL, an OCT signal also contains information about light attenuation within biological tissues;(70, 71) according to the Beer–Lambert law, light attenuation inside tissues is exponential. The slope of this distribution is proportional to the total

attenuation of ballistic photons. Since absorption in tissues is substantially less than scattering in the near-IR spectral range, the exponential attenuation is dependent mainly on the scattering. (72) Therefore, by analyzing the exponential profile of light attenuation detected by the OCT system, one can obtain information on tissue scattering properties. It has been suggested that localized analysis of the OCT signal may increase the clinical potential of OCT by allowing quantitative discrimination between different tissue types or their health state.(73) To date, few studies have focused on OCT signal patterns and *n* values in relation to regional structural orientation of enamel and dentine. The aim of this study was to use an SS-OCT system to evaluate *n* of human enamel and dentine obtained with different structural orientation of enamel prisms and dentinal tubules, and also to estimate changes in OCT signals as a result of variations in the structure of enamel and dentine. The null hypotheses were that local variation in the structure of enamel and dentine did not give rise to change in calculated *n*, and that OCT signal pattern is not significantly affected as a result of these structural variations.

Materials and methods

Tooth preparation

Twenty-eight non-carious human third molars that had no visible evidence of caries and crack or fracture were collected after the individuals' informed consent was obtained according to a protocol approved by the Institutional Review Board of Tokyo Medical and Dental University.

All the teeth were extracted for orthodontic reasons from male and female subjects with an age range of 20–25 years. After extraction, the teeth were stored at 4 °C in saline saturated with a 0.02% thymol until the experiment. A low-speed diamond saw (Isomet, Buehler, Lake Bluff, IL, USA) was used to slice the teeth into discs with thickness of 300–400 μm.6 Fourteen teeth were sectioned perpendicular to the long axis of the tooth at cuspal and mid-coronal regions (transverse sections), and the other 14 teeth were cut parallel to the long axis at the central fissure (sagittal sections).

Investigated enamel and dentine regions

Enamel with cross-cut prisms was studied on the cuspal enamel regions of transverse sections, and enamel with long-cut prisms was studied on the sagittal sections. Fig. 1 shows tooth regions and sectioning directions.

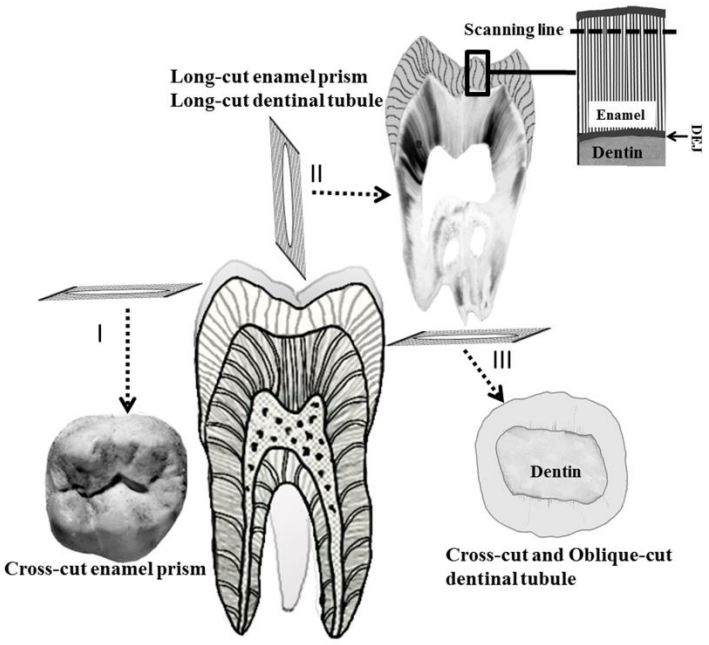

Fig. 1. Schematic illustration of human molar enamel and dentine prepared for *n* measurement. (I) Transverse section at the cusp used to obtain cross-cut enamel prism. (II) Sagittal section at central fissure in order to get long-cut enamel prism and long-cut dentinal tubule. The magnified area represents scanning direction for long-cut enamel prism. DEJ points at the dentine-enamel junction. (III) Transverse section at the mid coronal portion performed to obtain cross-cut and oblique-cut dentine tubule.

Each of the samples was placed on top of an unpolished metal plate in order to acquire B-scan images by OCT. A schematic of the system (Dental SS-OCT, Prototype 1, Panasonic Healthcare, Co., Ltd, Ehime, Japan) used in this study was shown in Fig. 2. The light source is a

commercially available scanning laser and sweeps in the near-IR wavelength at a rate of 30-kHz over a span of 100 nm centred at 1330 nm.

Axial resolution of the system is 12 μm in air, which corresponds to 8 μm in a tissue assuming an *n* of about 1.5. The lateral resolution of 20 μm is determined by the objective lens at the hand-held probe designed for intra-oral imaging. The acquired 2D OCT image size is 2000 × 1019 pixels, and pixel dimensions of 9 μm × 2.5 μm. This system employs a CMOS camera for real-time photographic imaging of a 10 mm × 10 mm surface area on the scanned sample, and is capable of acquiring serial 2D sections (B-scans) to construct 3D scans. The hand-held scanning probe connected to the SS-OCT was set at a fixed distance over the sample's surface, with the scanning beam oriented approximately 90° with respect to the surface.

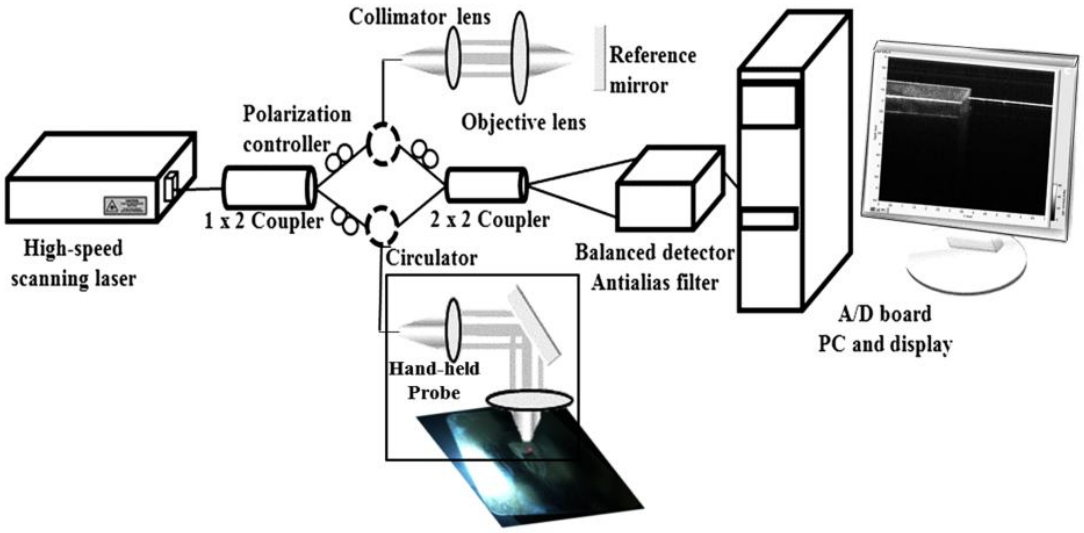

Fig. 2. The light output from a high-speed scanning laser is divided into reference arm and sample arm with a fiber splitter. Reference light and back-scattered light from the sample is recombined with a second fiber coupler to create the interferogram in time. Fringe response is detected with a balanced detector, converted to electrical signal and digitized by analogue-to-digital (A/D) board. Software constructs a 2D image from the signal after Fourier transform.

Fig. 3(b) is a photographic image obtained from CMOS camera attached to the scanning probe showing an *in vitro* tooth slice subjected to OCT imaging.

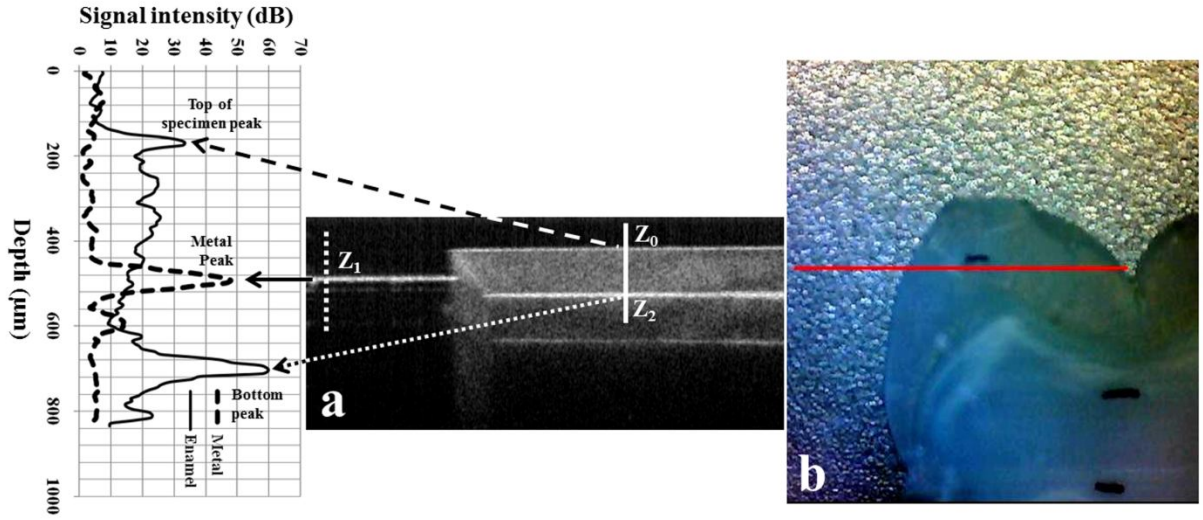

Fig. 3. Regional *n* calculation by OCT. (a) B-scan image and corresponding signal intensity profiles on marked locations for metal and enamel. Z_0 and Z_2 represent top and bottom of specimen from which the OPL was calculated while Z_1 shows the location of metal stage. The *n* was calculated by dividing the OPL over the true thickness or $(Z_2 - Z_0)/(Z_1 - Z_0)$. (b) Photographic CMOS camera image of the *in vitro* long-cut enamel slice presented in (a). The B-scan was obtained along the demarcated line.

Measurement of n

The *n* values were obtained following the OPL matching method; as shown in Fig. 3(b), a B-scan along the direction marked with a line was taken to obtain the 2D OCT image in Fig. 3(a). The lines which represented the reflected light from the upper surface of the sample and the metal plate without the sample were Z_0, and Z_1 respectively, and finally Z_2 represented the position of the reflector (metal plate) imaged through the tissue. The thickness of the sample could be determined by subtraction of the vertical position of the reflector (metal plate) outside

the tissue (Z_1) from the vertical position of the sample surface (Z_0) in the OCT image, and the additional OPL delay can be measured by subtraction of the vertical position of the reflector imaged through the tissue (Z_2) from the vertical position of the sample surface (Z_0). Image analysis software (ImageJ 1.42q; National Institutes of Health, Bethesda, MD, USA) was used to perform OCT image analysis.

Assuming the OPL in the sample is $Z_2 - Z_0$ and the actual thickness (t) of the sample is $Z_1 - Z_0$, we can obtain *n* of the tooth slices (sample) using Eq. (1) as

$$n = \frac{OPL}{t} = \frac{Z_2 - Z_0}{Z_1 - Z_0} \tag{1}$$

Eq. (1) was used to calculate the *n* at each location on average signal intensity profiles as shown in Fig. 3(a). Each value was calculated using an average profile obtained on an area (10 pixels or 25 μm in width) on the sample. Five areas were randomly selected on the region to be evaluated on each slice, from which average *n* of the region on that tooth slice was calculated. In this manner, values obtained for each of the regions on 14 teeth were used in the statistical analysis (n = 14). It was

difficult to detect the inferior border of dentine especially in (oblique-cut or long-cut dentine tubules), where a bottom peak with a sharp apex (metal stage reflection) was not detected within the area of interest (10 pixels or 25 μm in width) as presented in Fig. 5(d). In such cases the OPL could not be found; therefore an absolute *n* value could not be calculated. Those subjects were excluded from the analysis.

OCT signal slope measurement

Average OCT signal intensity profiles obtained for *n* measurement over each area were used for further analysis. The OCT signal slope (OCTSS) was calculated in a depth ranging from surface area of the specimen up to an optical depth of approximately 400 μm (depending on the sample thickness) using exponential fit of the slope of the profile as in Fig. 6(a) and (b).(69) The surface peak caused by Fresnel reflections at the interface of tissue and air(54, 63) and the bottom peak due to specular reflection from metal stage surface were excluded from the analysis by 50 μm from peak apex.

Microscopic imaging of the cross-sections

The actual orientation of enamel prisms and dentinal tubules at each region were confirmed under scanning electron microscopy (SEM). For this purpose, the slices were gently reduced using wet silicon carbide papers up to the same cross-section that had been imaged by OCT. In order to enhance the visibility of enamel prism orientation, the surface was treated by phosphoric-acid etching (35% for 15 s), rinsed with water, and air-dried. Dentine slices were further polished with diamond pastes down to 0.25 μm in particle sizes under running water. All the specimens were air-dried for 24 h in the room temperature (23 °C), sputtered with gold and viewed under the SEM (JSM-5310LV, JEOL, Tokyo, Japan) at 1500× magnification with an accelerating voltage of 20 kV.

Statistical analysis

Data were first probed to confirm normal distribution and homogeneity of variance among groups. In order to determine if there were significant differences in the local refractive indices and OCTSS

for cross-cut and long-cut enamel, the data were analyzed using T-test and Mann–Whitney U tests, respectively. Results of dentine were analyzed by one-way ANOVAs to compare between long-cut, cross-cut and oblique-cut dentinal tubule orientations with the Tukey's HSD and Games-Howell post hoc tests for *n* and OCTSS, respectively. Finally, t-test and Mann–Whitney U tests were carried out to determine significant differences in overall *n* and OCTSS between enamel and dentine. The significance level for all the statistical analyses was set at $\alpha = 0.05$ and the analysis were performed in the SPSS software (ver. 16, SPSS Inc., Chicago, IL, USA).

Results

Fig. 4 represents OCT B-scan images of cross-cut and long-cut enamel surfaces with corresponding SEM images of the enamel cross-sections after etching. Strong and homogenous signal intensity through enamel depth could be detected, and the metal reflection at the inferior border of enamel was readily detected on the intensity profiles.

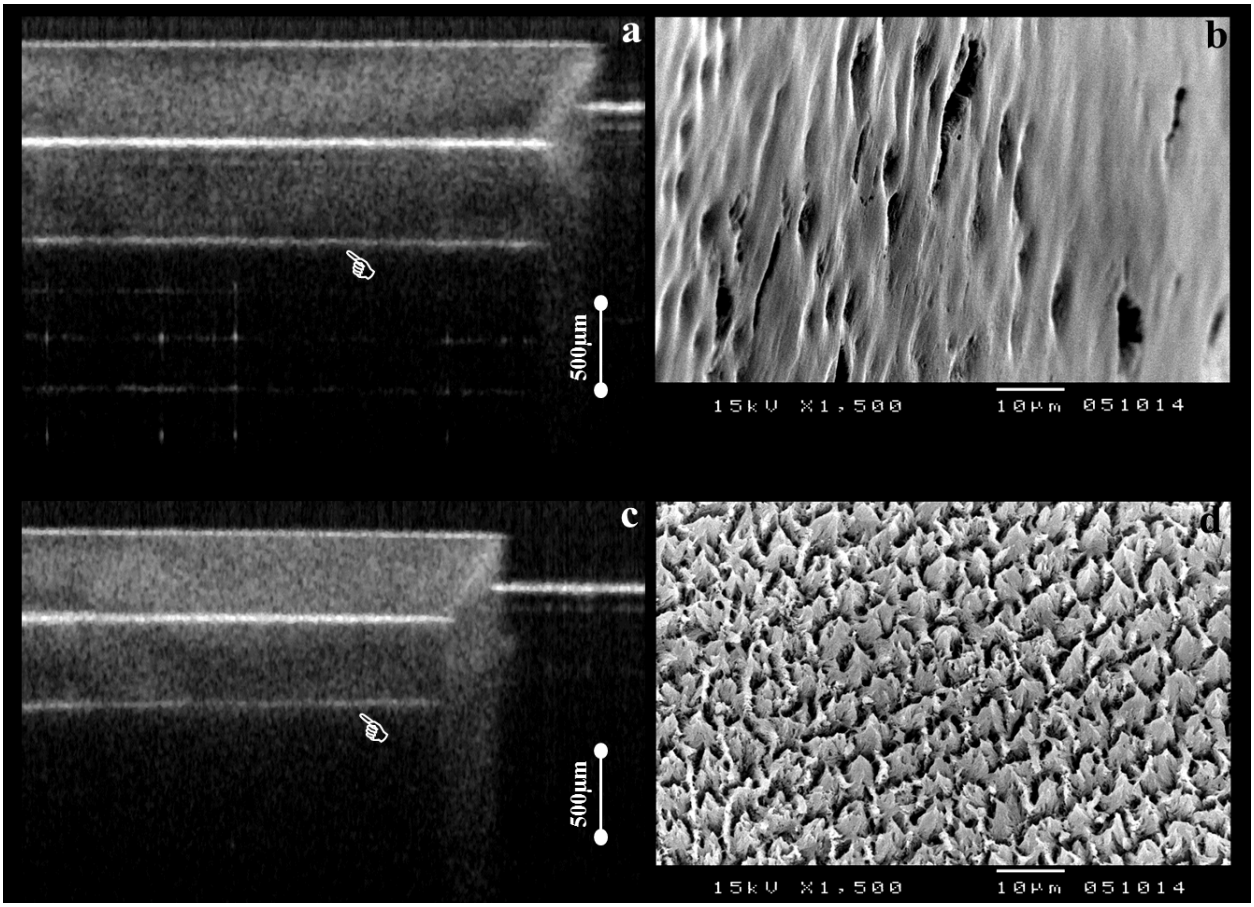

Fig. 4. OCT images and corresponding SEM micrographs of enamel slices. (a) and (c) OCT B-scan images of enamel slices with enamel prism orientation cross-cut and long-cut to the cutting surface respectively. The second lines (hand pointers) are due to mirror reflections between the metal and the enamel surface. (b) and (d) cross-sectional observation of phosphoric acid-etched enamel using SEM corresponding to the tomographic images, showing the enamel prisms orientation. A honeycomb pattern is clearly observed on long-cut enamel specimens (d). Note that the SEM images represent the enamel structure after cross-sectioning of the tooth slices along the same direction as OCT scan. The vertical bars show optical distance.

On the other hand, the appearance of dentine sections was different. Representative OCT images of mid-coronal dentine with their corresponding SEM cross-sectional observations on a sagittal section including both long-cut and oblique-cut dentine tubules are presented in Fig. 5(a)–(c). Fig. 5(d) and (f) shows OCT images of dentine samples

with corresponding SEM cross-sectional observation on a transverse mid-coronal section of cross-cut dentine tubules. The bottom of several dentine slices appeared as a curved feature under OCT. Fig. 5(e) shows A-scan signal intensity profile of oblique cut dentine tubules (white arrow).

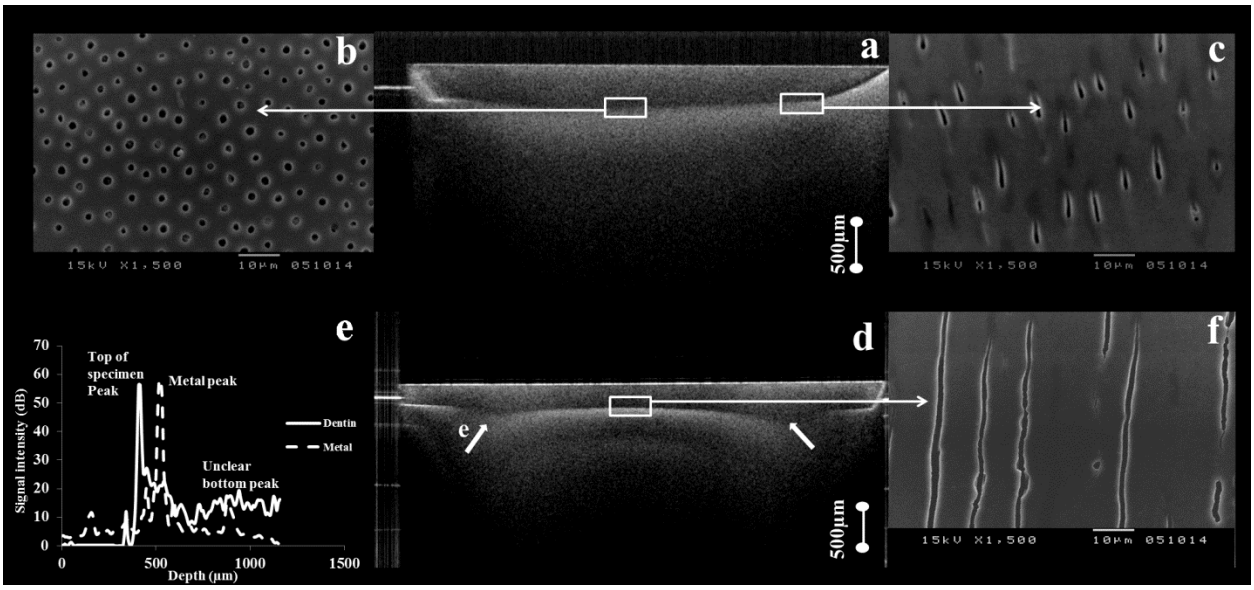

Fig. 5. OCT images and corresponding SEM micrographs of dentine slices. (a) OCT image of dentine on a sagittal section of tooth. (b) and (c) SEM observation of the areas demarcated on the cross-section shown in (a). At the center of specimen, the tubules are long-cut (perpendicular to the light beam direction) as confirmed by SEM in (b). At the sides, the tubules tend to be cut obliquely (c). (d) OCT image of dentine on a mid-coronal transverse section. (f) SEM observation of the areas demarcated on the cross-section shown in (d). At the center of specimen the tubules are cross-cut (parallel to the light beam direction) as confirmed by SEM in (f). Note that in the OCT image (d), the bottom line of dentine placed on the metal stage could not be readily recognized perhaps due to strong and complex scattering pattern of light (white arrows). (e) Signal intensity profile of the area pointed with the white arrow shows unclear bottom peak in oblique-cut dentine tubules. A dome-shaped reflection was observed at the bottom of this slice in OCT image, suggesting variable refractive indices within the tissue. The vertical bars show optical distance.

Representative A-scan signal intensity profiles of enamel and dentine are presented in Fig. 6(a) and (b) respectively. The slope of exponential fit of the OCT signal profile in these plots represented the OCTSS. The average signal slope appears to be higher in dentine than in enamel, indicating that loss of signal is more rapid in dentine compared to enamel.

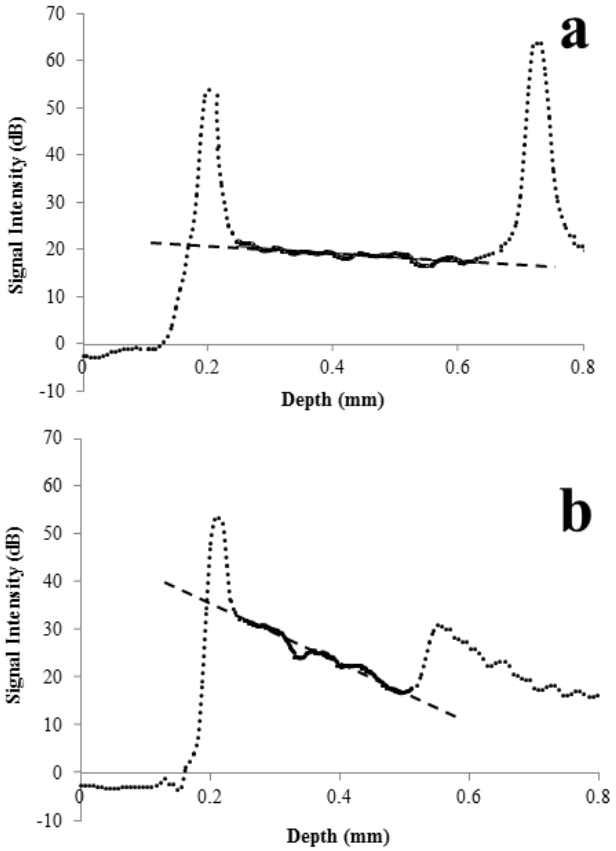

Fig. 6. Representative OCT signal intensity (A-scan) plots averaged over an area of interest on human enamel and dentine. Dashed line represents the exponential fitted line to the OCT signal from surface to the depth of sample (approximately 400 µm); this slope was recorded as OCTSS, so that the analyzed OCT signal excluded the surface and bottom peaks by 50 µm from the apex of each peak (solid line); (a) cross-cut enamel sample, y = 23.4e−0.48x, OCTSS = 0.48, R2 = 0.75, (b) long-cut dentine sample, y = 59.7e−2.39x, OCTSS = 2.39, R2 = 0.94. Note that the bottom peak in (b) is wider than that in (a) due to diffuse scattering in dentine.

The resulting average *n* and OCTSS values for each region on enamel and dentine were presented in Table 1. No significant difference was found in any of the variables between cross-cut and long-cut enamel

groups ($p > 0.05$). In dentine, there was a significant difference in *n* and OCTSS among different regions. In cross-cut tubule orientation, the average *n* and OCTSS values were lower compared to other two groups (long-cut and oblique-cut), and the difference was statistically significant ($p < 0.05$).

Table 1. Local *n* and OCTSS of Enamel and Dentin

	Enamel		Dentin		
Orientation	**Cross-cut**	**Long-cut**	**Cross-cut**	**Oblique-cut**	**Long-cut**
n	**1.63±0.02** [a]	**1.62±0.02** [a]	**1.49±0.07** [b]	**1.56±0.08** [c]	**1.60±0.04** [c]
Average *n*	**1.63±0.02** [d]		**1.55±0.08** [e]		
OCTSS	**0.26±0.44** [a]	**-0.08±1.44** [a]	**1.37±0.42** [b]	**2.64±1.01** [c]	**2.31±0.87** [c]
Average OCTSS	**0.07±0.69** [d]		**2.15±0.98** [e]		

[a,b,c,d,e] **In each row there was no significant difference between values denoted by the same superscript letter (P>0.05).**

Adding all data from enamel and dentine groups, average group refractive indices of enamel and dentine were calculated as 1.63 and 1.55 respectively. As for average OCTSS, the values were 0.07 and 2.15 for enamel and dentine, respectively (Table 1). There was a significant difference in both variables between enamel and dentine ($p < 0.05$).

Discussion

Our aim in the current study was to investigate the changes in *n* of enamel and dentine in different regions induced by different orientation of enamel prisms and dentinal tubules, respectively. Presently, two successful methods have been proposed for determining the *n* of biological tissues by OCT, namely the focus-tracking method and the OPL matching method. The former is based on the coherence gating properties of OCT to track the focal position as the sample is moved along the optical axis, which may be suitable for *n* measurements *in vivo*. The second method uses the ability of OCT to measure the OPL matching during an OCT scan for *in vitro* measuring of the *n*.(68) In this paper, the *n* was calculated with the second method, which has the advantages of simple and fast measurement, and higher accuracy compared with the focus-tracking method.(49)This methodology requires cross-cutting of the sample; further developments are required for measurement of *n* in dental hard tissues *in vivo*.

While interpreting the results of this study, it should be noted that the architecture of enamel and dentine is more complicated than the orientation categories assumed in this study. The description of orientation in this study was in two dimensions; however, in reality the micro-architectures of prims and tubules are three-dimensional. In order to ensure the regional orientations assumed for each subgroup in this study, microscopic observations were carried out.

Although enamel groups demonstrated different levels of morphological patterns under SEM, in this study cross-cut and long-cut enamel groups showed similar *n* values. The results can be explained by a closer look into human enamel structure; fully developed mature dental enamel is a highly organized structure of enamel prisms with 4–6 μm transverse dimensions, which mainly consist of bundles of nanorod-like HAp crystals. Each of the densely packed crystals in a prism has six neighbours and is aligned along the principal growth direction of the prism.(65) Considering the regular HSBs pattern in enamel, it was suggested that the prismatic structure of enamel had evolved to optimize resistance to attrition, abrasion and fracture of the tooth. Certain aspects

of this structure have beneficial roles in clinical techniques such as bonding, and should be considered thereby.(41, 59, 60) Optically, there are two types of scatterers in enamel; the small enamel crystallites that produce Rayleigh-like isotropic distributions, and the large enamel prisms which are optically uniaxial.(63, 73-75) Results of the current study suggest that the regular structural orientation of the enamel resulted in similar OPLs in both cross-cut and long-cut prism groups. Moreover, it appears that the prism orientation responsible for appearance of HSBs did not affect *n* values measured significantly. Besides, the HSBs in enamel previously observed by a polarisation-sensitive OCT(45) could not be detected by OCT without polarisation sensitivity in the present study. In addition to *n*, OCTSS results were also not significantly affected by regional prism orientations, further confirming homogeneity of enamel optical properties under OCT. It is noteworthy that the loss of signal (OCTSS) was very small for enamel, in accordance with previous reports on enamel transparency at this wavelength range; near-IR.(64)

Dentine has a more complex structure and consists of three main components: minerals (primarily HAp), a collagen-based organic matrix, and tubules permeating the entire volume of the dentine. HAp crystals of dentine are smaller than those of enamel. The main dentine structural component is micrometre-sized dentinal tubules, which radiate with an S-shaped curve from the pulp cavity towards the periphery. Tubule attributes (diameter and density) are greatly variable among dentine depths, teeth or subjects. In the deeper portion of the dentine near the pulp, the tubule diameter is 3–4 μm, with number density of 7.5×10^4 per square mm; in the shallower portion near the DEJ, tubules are narrow, with a lower density of approximately 3×10^4 per square mm.(62) Moreover, the peritubular dentine differs from the intertubular dentine by a higher concentration of the mineral component. The scattering processes in dentine are mainly differentiated by two types; (1) symmetrical processes around the incident beam caused by mineral crystals and collagen fibrils; (2) the processes centered asymmetrically, caused by the oriented tubules.(63)

Several studies,(62, 76, 77) have investigated the role of tubules in scattering and transport of light. It is widely agreed that light propagation in human dentine exhibits a strong directional dependence, with the tubules playing a dominant role. Researchers assumed that light guiding along the tubules was due to the waveguide or fiber-optic effect, where light could propagate inside the tubules based on the principle of internal reflection that occurs when light is passed through a transparent cylinder composed of an inner core (the tubule space, whether it contains water, air, or dentinal fluid) with different refractive indices.(78) Some other researchers have challenged the fibre-optic theory; Kienle et al.(77) explained that if the angle between the direction of the light beam and the dentinal tubule was small, light was guided along the tubules in a direction close to that of the tubule due to multiple-scattering by the tubules rather than the fibre-optic effects assumed previously. Zolotarev et al.(74, 79) suggested that the orientation of the uniaxial HAp crystals in the tubule resulted in the tubule behaving like uniaxial crystals with anisotropy of the optical properties of the tubule themselves and different *n* along the axes of the

tubules and transverse to them. They suggested that the waveguide effect did not take place in dentine sections mainly due to the strong suppression of the process by scattering in the intertubular dentine.

In dentine groups in the current study, a significant decrease in *n* was detected at locations with cross-cut tubules, where the dentinal tubules were parallel or made a small angle to the direction of the light beam, compared to the other two groups. The result indicated that the light guiding effect of the cross-cut dentinal tubule located at the central portion of the mid-coronal transverse sections resulted in a shorter OPL. In the case of oblique-cut or long-cut dentine tubules, the result was different. In this case, the collagen-HAp was mainly responsible for light propagation with the dentinal tubules acting as spaces filled with a low-n medium (air, water, or intratubular fluid), leading to a longer OPL.(77, 78) With the strong and diffuse backscattering at the bottom of some human dentine sections in this study, it was occasionally difficult to detect the inferior border of dentine (as reflection from metal), especially at locations with oblique-cut or long-cut dentine tubules, as presented in

Fig. 5(d). This phenomenon maybe a result of random scattering of light where the incident light had a larger angle to the dentinal tubules.

Moreover, the OCTSS increased for oblique-cut and long-cut dentine tubules compared to the cross-cut group. This finding indicated smaller attenuation of light, probably due to the light guiding property of the tubules in cross-cut group. It appeared that the change of scattering with the change in structural orientation in dentine had resulted in a variable *n*. In addition, it is suggested that one might roughly predict local structural orientation of sound dentine from OCT signal patterns.

Physical attributes of the tubules and dentine may change due to ageing and sclerotic alterations which will affect light propagation patterns and optical properties of the tissue.(80) Other factors such as subject's gender and anatomy of the tooth (e.g. anterior vs. posterior) may also affect the microstructure of the dentine; and presumably its optical properties.(81) Further work on optical properties of dentine needs to be carried out considering these factors.

The overall average *n* results in Table 1 are coincident with the results previously measured by Meng et al.(49) Kienle et al.(77) and Ohmi et al.

(82) Standard deviations for enamel *n* in the current study were considerably higher than those reported previously.(49) The standard deviations may reflect differences in natural biological samples obtained from several subjects as opposed to synthetic substrates, or several slices obtained from the same tooth. Moreover, the optical resolution of the device (12 μm in air), when considering the thickness of slices (300–400 μm) may also affect the variance of OPL measurements.

Under clinical examination of coronal dentine, light must first pass through the full thickness of the enamel before it reaches the dentine. Since the attenuation of light in sound enamel is relatively small and is not significantly affected by its structural orientation, the signal from underlying dentine would still carry significant information. Moreover, there is no enamel covering root dentine and the cementum is worn out in exposed parts,(83) in which case light can penetrate through dentine directly.

In addition to vital information of structural variations in the tissue, from a clinical point of view, the study of *n* has at least two major implications; structural depth and thickness have to be measured

precisely for both diagnostic and operative purposes in dentistry, i.e. measurement of the remaining dentine thickness over the pulp is important while preparing a cavity for dental restorations.(84) In addition, *n* bears diagnostic information as dental demineralization induces local changes in the *n*;(54, 85, 86) therefore, these records of refractive indices may be important for detection of dental caries in the future. Further research on these optical properties is needed for demineralized tissue and after remineralization of carious lesions.

Conclusion

It was demonstrated that OCT is a useful tool for investigation of optical properties of human dental tissue and from which additional physical parameters such as *n* and OCTSS may be derived in addition to cross-sectional imaging. Enamel showed small OCTSS; unlike enamel, anisotropic structure of dentine and orientation of dentinal tubules affected light propagation pattern and OPL resulting in different refractive indices and OCTSS values. A prior knowledge of these

features and their relations with the histology and pathology will provide verification of the diagnostic power of OCT.

Acknowledgments

This research was supported partly by the Grant-in-Aid for Scientific Research (No. 22791924) from the Japan Society for the Promotion of Science, partly by the Research Grant for longevity sciences (21A-8) from Ministry of Health, Labor and Welfare, and partly from the Global Center of Excellence Program, International Research Center for Molecular Science in Tooth and Bone Diseases at Tokyo Medical and Dental University.

Chapter 3

Relationship between refractive index and mineral content of enamel and dentin using SS-OCT and TMR

Introduction

Development of non-invasive medical diagnostic techniques has received a great amount of attention nowadays. Wherever possible, an attempt is made to abolish and replace invasive methods in favour of others that provide similar results without having a negative impact on the tested object. A significant role among them is played by optical diagnostic techniques.(53, 55, 87)

Optical coherence tomography (OCT) has become critically important in medical field since this technique can provide non-invasive diagnostic images. OCT enables cross-sectional imaging of internal biological structures by differentiating between scattered and transmitted or reflected photons using broad-band, near-infrared (near-IR) light sources with micron scale resolution. In dental science, OCT is a useful

imaging technique for assessing early caries, oral cancer, and periodontal diseases. (54, 88)

More recently, the swept source OCT (SS-OCT) system has been developed as an implementation of spectral discrimination, in which the laser light source sweeps the near-IR wavelength at a high rate. The mechanical scanning at the reference mirror has been eliminated since the SS-OCT time-encodes wave number by rapidly tuning a narrowband source through a broad optical bandwidth. These characteristics enable SS-OCT to obtain images in a shorter time and superior performance with respect to detection sensitivity by means of improving the signal to-noise ratio 2 to 3 orders of magnitude over conventional OCT. (56, 89)

One of the most important optical properties of a highly scattering biological tissue is the *n*, which is an important parameter of light propagation in biological tissues including teeth. Indeed, scattering is the end result of local *n* variation.

OCT is based on low-coherence interferometry and thus, can be used to measure the optical thickness of a sample. Since the optical thickness is

the product of the n and the geometric thickness, if the thickness of the sample is known, the group index can be calculated from the group delay. (67)

n is a physical property of a material or substance mathematically defined as:

$$n = \frac{V_v}{V_m} \qquad (1)$$

Where, n = refractive index of mineral, V_v = velocity of light in a vacuum, V_m = velocity of light in the mineral.

This relationship shows the impact of density or specific gravity to the index of refraction in that the greater the density the slower the speed of light. Thus, higher density materials will have higher *n* and vice versa.

Generally, dental caries is considered as a partial chemical dissolution of apatite crystals in dental hard tissue. Recent studies elucidated the caries process involves not the dissolution but also remineralization of the dissolved minerals, implying 3 types of minerals being present in the carious lesions, undissolved, dissolved and possibly

remineralized or recrystallized minerals. It is reported that properties of the remineralized minerals are different from the original in terms of crystallinity (size, purity). Quantitative determination of *n* of human tissue using OCT is a simple method that can provide information on tissue structure in health and disease within the sample. Therefore the accurate measurement of the changes in a tooth' s *n* after de-/remineralization may give us useful information to predict changes in the subsurface structures, quantitative assessment of mineral loss, and remaining enamel and dentin thickness.

The aim of this study is to investigate relationship between *n* measured by OCT and mineral content (MC) evaluated by TMR of enamel and dentin. The null hypotheses tested are (1) *n* does not change significantly based on variation on MC. (2) there is no correlation between *n* determined by OCT and MC calculated by TMR.

Swept Source Optical Coherence Tomography

The SS-OCT system (OCT-2000, Santec, Komaki, Japan) used in this study is a frequency domain OCT technique in which the probe

power is less than 20 mW, within the safety limits defined by American National Standards Institute. The light source in this system sweeps the wavelength from 1260 nm to 1360 nm at 20 kHz sweep rate with central wavelength at 1319 nm. The focused light-source beam is projected onto the sample and scanned across the area of interest in two dimensions (x, z) using a hand-held probe. Backscattered light from the subject is coupled back to the system, digitized in time scale and then analyzed in the Fourier domain to reveal the depth-resolved reflectivity profile (A-scan) at each point. The combination of a series of A-scans along the section of interest creates a raw data file (Bscan) with information on the signal intensity (backscattered light) and x, z coordinates from each point within the scanned area. Two-dimensional cross-sectional images can be created by converting the B-scan raw data into a grayscale image. Axial resolution of the system is 11 μm in air, which corresponds to 8 μm in a tissue assuming an *n* of about 1.5. The lateral resolution of the system 17 μm is determined by the objective lens at the probe.

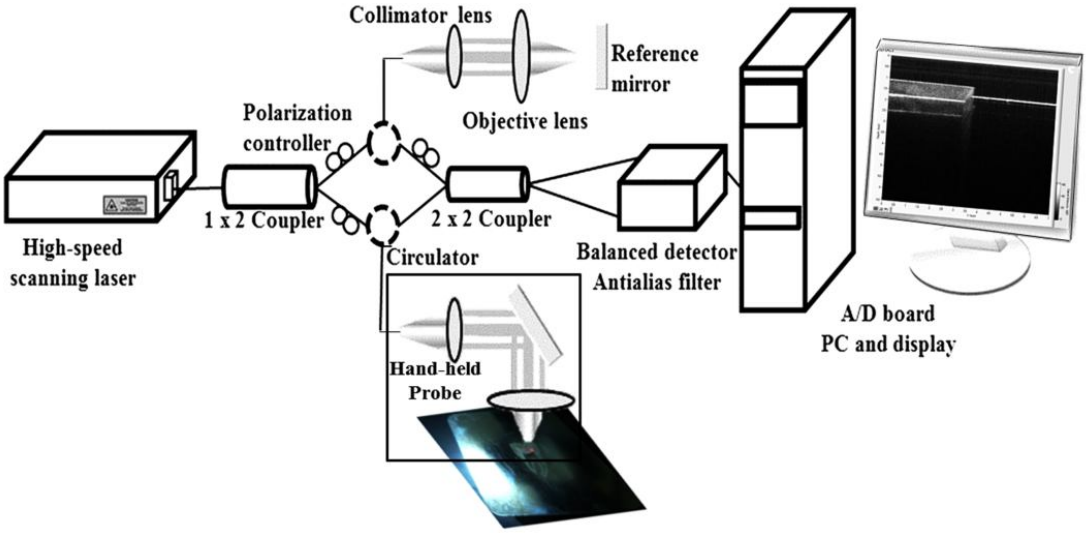

Figure 1. Schematic illustration of the Santec SS-OCT system. The sample arm is a hand-held scanning probe capable of scanning in 2D (x, z) and 3D (x, y, z) modes in maximum dimensions of 15 x 6.6 and 15 x 15 x 2.6 (mm), respectively.

Experiments and Results

Specimen Preparation

Bovine maxillary incisors were carefully chosen and stored frozen prior to the experimental procedure. Enamel and dentin blocks (≈ 7 × 7 × 3 mm^3) were cut out and mounted in resin (GC, Tokyo, Japan). The blocks were polished on wet polishing paper (lapping paper 800, 1,200 and 2,000grit, by 3M ESPE, St. Paul, MN, USA) to expose a sound and flat

enamel and dentin surface with mirror polishing. For each block, sound, demineralized, and remineralized zones were then made on the same enamel and dentin surface as follows: the middle partition of each sample was covered with a thin layer of acid-resistant nail polish (red nail polish; Revlon, New York, USA) that served as the control groups. Two windows on each sample were exposed to the demineralization solution, and one window was exposed to the remineralization solution. OCT images were taken as control before the demineralization.

Demineralization and Remineralization

The specimens were demineralized in a demineralizing solution 1.5 mM $CaCl_2$, 0.9 mM KH_2PO_4, 50 mM acetic acid, 3.08 mM NaN_3, 0.3 ppm F as NaF (for the creation of subsurface lesion), (pH adjusted to 4.5 by NaOH) for two months and then treated by remineralizing solution consisting of (1.0 mM $CaCl_2$, 3.0 mM KH_2PO_4, 3.08 mM NaN_3, 20.0 mmol/L cacodylate buffer maintained at pH 6.5) for 2 months. 0.7 ppm F as NaF was added into remineralization solution to enhance remineralization.

n measurement:

A low-speed diamond saw (Isomet, Buehler, Lake Bluff, IL, USA) was used to slice the samples into disks with thickness of 300 µm to 400 µm.(49, 90) Cut-enamel and dentin slices were placed on top of an unpolished metal plate in order to acquire B-scan images. The hand-held scanning probe connected to the OCT system was set at 5 cm distance from the specimen surface, with the scanning beam oriented about 90° to the surface. A custom made jig was mounted on a micro meter stage to keep each specimen surface parallel to the probe plane. The cross-sectional images were acquired at depths 0, 20, 40, 60, 80, 100, 120 and 140 µm depths in enamel and 0, 40, 80, 120, 160, 200, 240, 280 and 320 µm depths in dentin (Figure 2).

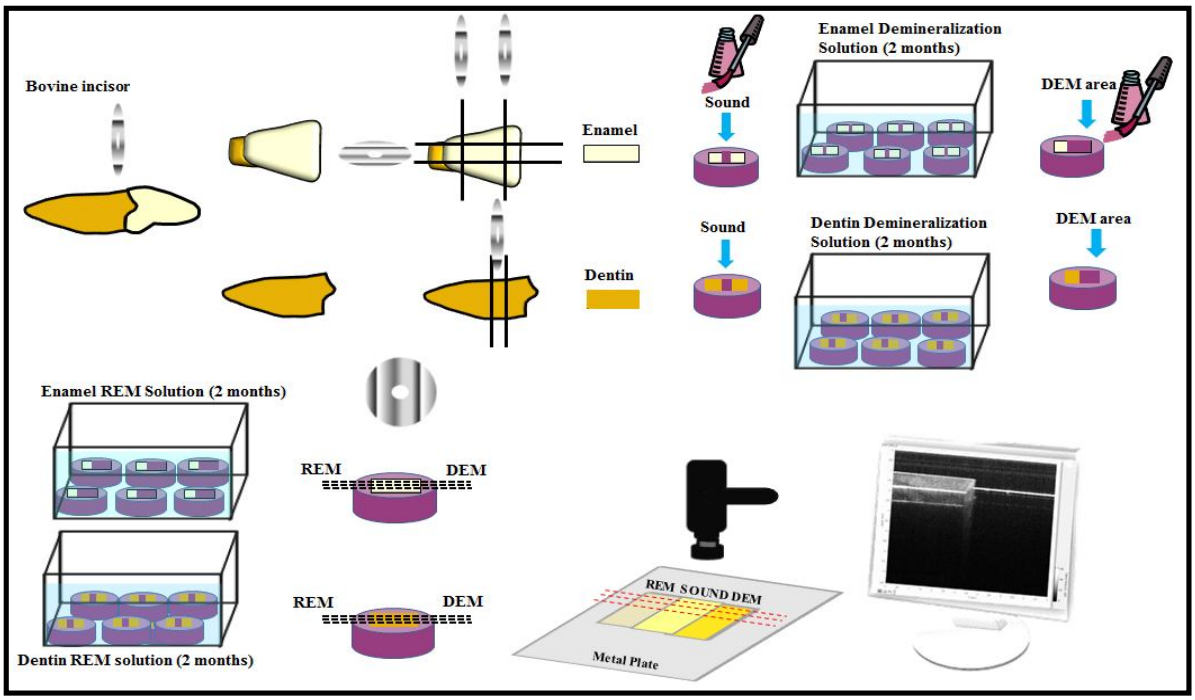

Figure 2. The schematic diagram of experimental setup (DEM= demineralized, REM=remineralized).

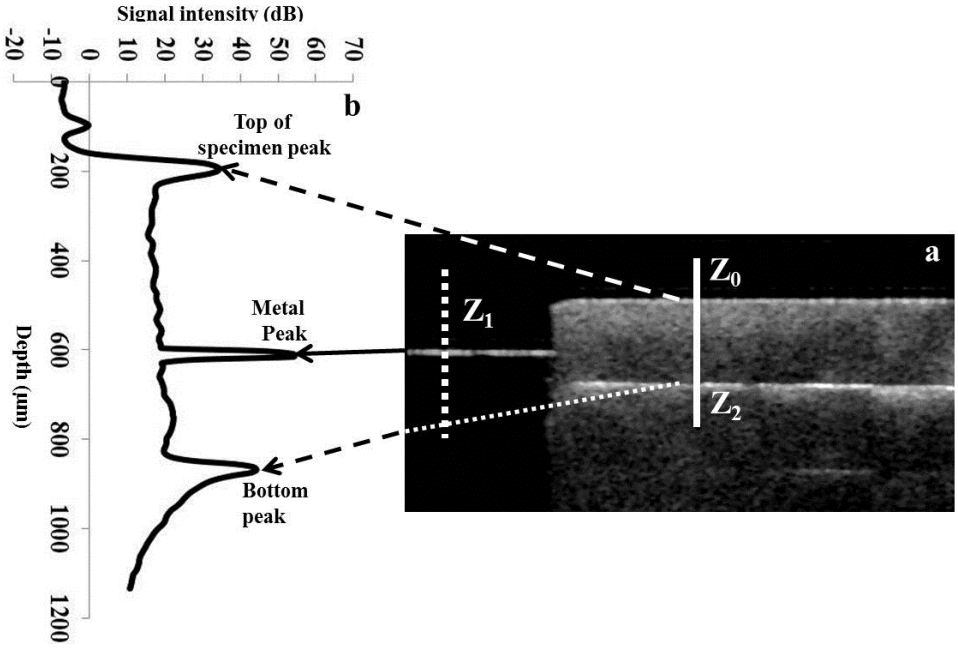

Figure 3. B-scan image (a) and corresponding signal intensity profiles (b). Z_0 and Z_2 represent top and bottom of specimen from which the OPL was calculated while Z_1shows the location of metal stage. The *n* was calculated by dividing the OPL over the true thicknessor $(Z_2 – Z_0) / (Z_1 – Z_0)$.

A water-based gel containing 2% hydroxyl ethyl cellulose (HEC, Wako Chemicals, Osaka, Japan) was placed on the tooth surface as an *n* matching medium and it was spread flat on the specimen surface using a micro brush to obtain a film thickness of approximately 100 μm. As shown in fig. 3 (a, b), a B-scan was taken to obtain the 2D SS-OCT image. Image analysis software (ImageJ 1.42q; National Institutes of Health, Bethesda, MD, USA) was used to perform SSOCT image analysis. The lines which represented the reflected light from the upper surface of the sample and the metal plate without the sample were Z_0, and Z_1 respectively, and finally Z_2 represented the position of the reflector (metal plate) imaged through the tissue. The thickness of the sample (t) could be determined by subtraction of (Z_1) from the (Z_0) in the SS-OCT image, and the additional optical path length (OPL) delay can be measured by subtraction of the (Z_2) from the (Z_0). Therefore, we can obtain n of the tooth slices (sample) using Eq. (2).

$$n = \frac{OPL}{t} = \frac{Z_2 - Z_0}{Z_1 - Z_0} \qquad (2)$$

Each value was calculated using an average profile obtained on an area (10 pixels or 25 μm in width) in each depth on the sample. Five areas were randomly selected and average *n* of these five areas was calculated on each tooth slice.

TMR Analysis:

The specimens were processed for analysis as follows; the enamel and dentin samples were dehydrated in ascending alcohol solutions (totally about 1h and 30 min), immersed in styrene monomer (2 h), and embedded in polyester resin (Rigolac, Oken, Tokyo, Japan) to prevent breaking the surface, the specimens then were more polished to obtain 120 μm thicknesses using polishing machine (ML-160A, Maruto Instrument, Tokyo, Japan). Dentin samples were polished a little to obtain 250 μm. TMR images were taken using an x-ray generator (SRO-M50; Sofron, Tokyo, Japan) at 25 kV voltage and 4 mA current for 20 min, with a Ni filter. The distance between the x-ray tube and the specimen was 15 cm. The TMR images, together with 15 aluminum step wedges (each 15 μm in thickness), were captured in the x-ray glass plate

film (High Precision Photo Plate PXHW, Konica Minolta Photo, Tokyo, Japan), and scanned as 8-bit digital images using a CCD camera (DP70, Olympus, Tokyo, Japan) attached to a microscope (BX41, Olympus). Mean mineral profiles (mineral density versus depth) were created using ImageJ and a custom Visual Basic application written in Microsoft Excel. The mineral density (vol.%) was calculated at the same depths as *n* measurement using the calibration curve, considering that the sound (non-demineralized) enamel and dentin contained 86 and 48 vol.% respectively.

OCT and TMR:

The *n* was plotted against MC for enamel and dentin separately. Pearson's correlation showed strong correlations between *n* and MC; r= 0.94, 0.97 in enamel samples and r=0.95, 0.91 in dentin samples after demineralization and remineralization respectively ($p < 0.05$) (Figure 4).

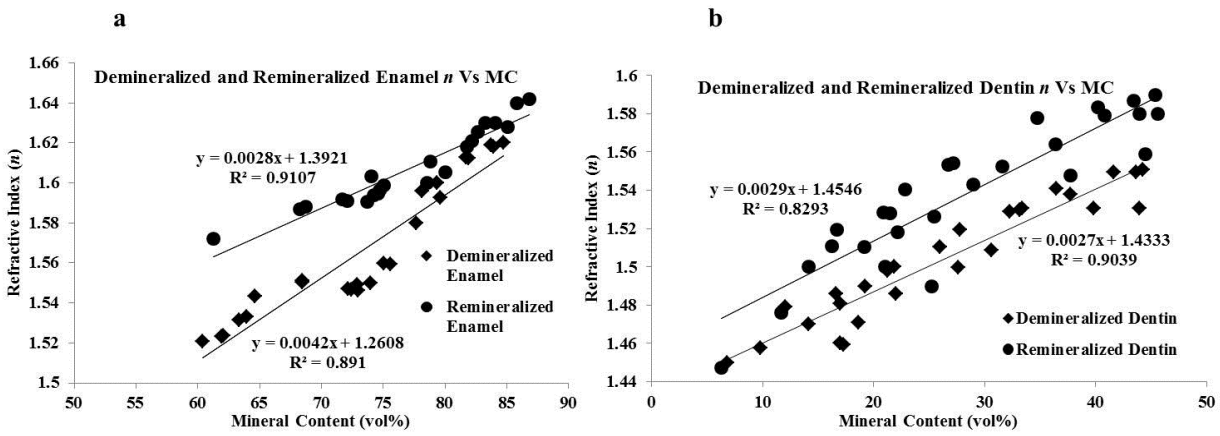

Figure 4. Graphs representing relationship between *n* and MC measurement (a, b). The *n* of the OCT was significantly correlated with the MC of the TMR measurements in enamel and dentin after demineralization and remineralization treatment respectively (r=0.94, 0. 0.97, and r=0.95, 0.91p < 0.05).

Conclusions and Future Directions

A laboratory methodology to trace mineral changes in enamel and dentin according to the refractive indices of hard tissue was validated in the present study using optical path length shifting method under OCT. This technique was sensitive enough to discriminate *n* changes based on the changes of the mineral density produced by the demineralization and remineralization treatment in the different depths and could be suitable for monitoring mineral changes *in vitro*. The same MC in remineralized samples corresponded to higher *n* values compared to

demineralized samples both in enamel and dentin, which may be due to different crystallographic structure after remineralization. Explanation for the differences between remineralized and demineralized enamel and dentin require further investigation of the factors involved. The potential clinical implication of the *n*-based mineral density assessment relies on further research to probe an intraoral methodology.

Acknowledgements

The works presented in this paper were supported by the grant from the Japanese Ministry of Education, Global Center of Excellence Program, International Research Center for Molecular Science in Tooth and Bone Diseases, the Research Grant for Longevity Sciences (21A-8) from Ministry of Health, Labor and Welfare and also Grant-in-Aid for Scientific Research (No. 22791924) from the Japan Society for the Promotion of Science.

Chapter 4

Estimation of Enamel and Dentin Mineral Content from Refractive Index

Introduction

Caries process is initiated by loss of minerals due to a shift of the dynamic balance between demineralization and remineralization. (91) A deep understanding of the changes induced by the process is a basic element of dental research. In terms of clinical dentistry, objective and quantitative means for early detection of changes and monitoring are of fundamental importance in the modern caries management strategies. Apart from the conventional visual, tactile and X-ray based methods, there is an increasing interest in new modalities for tissue characterization and diagnosis. Dental hard tissues are scattering media, and their optical properties carry diagnostic information; recent technological advances in the field of optics have enabled accurate measurement of optical tissue properties using high-resolution imaging

devices. (46, 92) Optical coherence tomography (OCT) is an interferometric technique enabling cross-sectional imaging of internal biological structures by differentiating between scattered and transmitted or reflected photons using broad-band, near-infrared (near-IR) light sources with micron scale resolution. (48) The non-ionizing imaging technique has found a great potential in dentistry for applications ranging from caries detection to assessment of defects within dental biomaterials and tissues using cross-sectional images. (53, 55, 88, 93)

n is an important parameter in light propagation through biological tissues including teeth. The *n* of the tissue can serve as an indicator of its scattering properties, as scattering itself is the end result of local *n* variation(67) Historically, this parameter was used to determine the purity of the enamel and dentin powders. (94) Conventional determination of *n* required immersion of the dental substance in fluids with the same *n* or the dispersion staining method. (95) An emerging class of *n* measurement methods employs low-coherence interferometry; on which principle OCT is based. OCT can be used to measure the optical thickness of a specimen, and thereby *n*. (67, 70)

OCT has been used to investigate the *n* of sound enamel and dentin, using the optical path-length (OPL) shifting approach which requires sectioning of the samples. (49, 90)

It was suggested that early demineralization caused by caries altered *n* of enamel. (85) It is also well known to the clinicians that the appearance of white-spot lesions after air-drying of the enamel surface is due to variation of *n*. (96) However, a quantitative relationship between *n* MC of enamel and dentin has not been previously examined. Thus, the aim of this study was to investigate the relationship between local *n* determined using OCT and MC of the same location measured on by transverse microradiography (TMR) on demineralized and remineralized enamel and dentin slices.

Materials and methods

Specimen preparation:

Figure 1 shows schematic diagram of the experimental setup; 10 enamel and 10 dentin blocks (7×7×3 mm3) were prepared from labial aspect or root region of a freshly extracted permanent bovine incisor

(aged 24±5 months) obtained according to institutional Animal Ethics Committee guidelines using a low speed diamond saw (Isomet, Buehler, Lake Bluff, Illinois, USA). Enamel and dentin surfaces of the resin-embedded bocks (Epoxycure resin, Buehler) were polished using 1500 grit silicon carbide (SiC) papers (Sankyo, Saitama, Japan) under running water. The polished surfaces were partitioned into three regions; the middle region was covered with a thin layer of acid-resistant varnish (Shiseido, Tokyo, Japan) to serve as the sound (control) region. The other two regions were subjected to demineralization at pH 4.5 for enamel and 4.7 for dentin at 37°C for two months respectively. One demineralized region on each specimen was covered with acid-resistant varnish, leaving the other one exposed for remineralization. The specimens were then placed in a remineralization solution (pH 6.5) at 37°C for another two months. The composition and degree of saturation (DS) of each solution are summarized in the Appendix Table. Finally, the diamond saw was used to cut the specimens through the center into slices 300 to 400 μm in thickness.

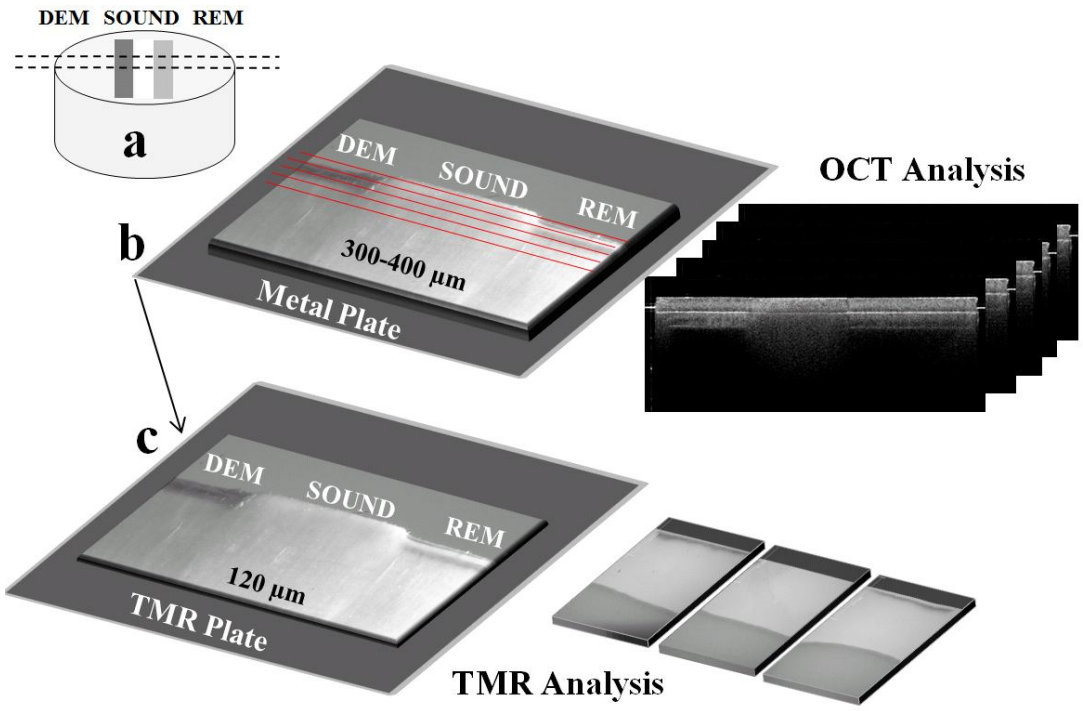

Figure. 1 (a) the setup of the swept source optical coherence tomography OCT for this experiment; light output from a high-speed scanning laser is divided into reference arm and sample arm with a fiber splitter. Reference light and back-scattered light from the sample is recombined with a second fiber coupler to create the interferogram in time. Fringe response is detected with a balanced detector, converted to electrical signal and digitized by analog-to-digital (A/D) board. Software constructs a 2D image from the signal after Fourier transform. (b) specimen preparation for the experiment; the bovine blocks with three regions of demineralized (DEM), remineralized (REM) and sound enamel or dentin embedded in resin were transversely sectioned to 300-400-µm thick slices; (c) the slices were placed on a metal plate and cross-sectionally scanned by OCT at various depth levels through the lesions; (d) the slices were further polished and subjected to transverse microradiography for mineral content assessment.

Appendix Table. pH and chemical composition of the treatment solutions.

Chemical composition	Enamel		Dentin	
	Demin	Remin	Demin	Remin
$CaCl_2$	1.5 mM	1.0 mM	1.5 mM	1.0 mM
KH_2PO_4	0.9 mM	3.0 mM	0.9 mM	3.0 mM
CH_3COOH	50.0 mM	20.0 mM	50.0 mM	20.0 mM
NaN_3	3.08 mM	3.08 mM	3.08 mM	3.08 mM
F as NaF	0.3 ppm	0.7 ppm	-	0.7 ppm
pH	4.5	6.5	4.7	6.5
DS (HAp)*	0.21	7.7	0.28	7.7
DS (Fluoroapatite)*	0.89	21.7	-	21.7

$CaCl_2$: Calcium chloride, KH_2PO_4: Potassium dihydrogen phosphate, CH_3COOH : Acetic acid, NaN3 : Sodium azide, NaF : Sodium fluoride, DS : Degree of Saturation.
* DS was obtained by a software provided by Forsyth Institute (Cambridge, MA, USA) with DS = $(IP/K)^{1/9}$, where IP and K are the ion activity products and solubility products of HAp and fluoroapatite, respectively.

n measurement:

The OCT-2000 system (Santec, Komaki, Japan) is a swept source (SS)-OCT technique operating at 1310 nm center wavelength. OCT interprets the magnitude of the light reflected from the subject into the depth-profile of the subject, as previously detailed.(54, 55) The axial resolution of this OCT system is 11 μm in air, and the lateral resolution (spot-size) of 17 μm is determined by the objective lens at the probe.

Enamel and dentin slices were placed on the top of a metal plate in order to acquire B-scan images. The hand-held scanning probe connected to the OCT system was set at 5 cm distance from the specimen surface, with the scanning beam oriented about 90° to the surface. For each specimen, 12 OCT cross-sectional images were acquired at 20 μm intervals from surface up to a depth 220 μm on the enamel slices, and at 40 μm intervals up to a depth 440 μm on the dentin slices in the form of 12 data sets (2000×1019 pixels) over the width and optical depth of 8×4 mm. A small amount of a water-based gel was placed over the tooth surface to prevent dehydration and reduce reflections from surface of the slices.(54) A detailed description of the OPL matching method for *n* measurement was given previously.(90) Briefly, as shown in Fig. 2(a) and (b), *n* at each depth level through the slice was calculated using an average profile obtained over a 50-μm-wide central area in each sound, demineralized and remineralized region on OCT images (n = 10). Average *n* profiles were plotted against depth in each region.

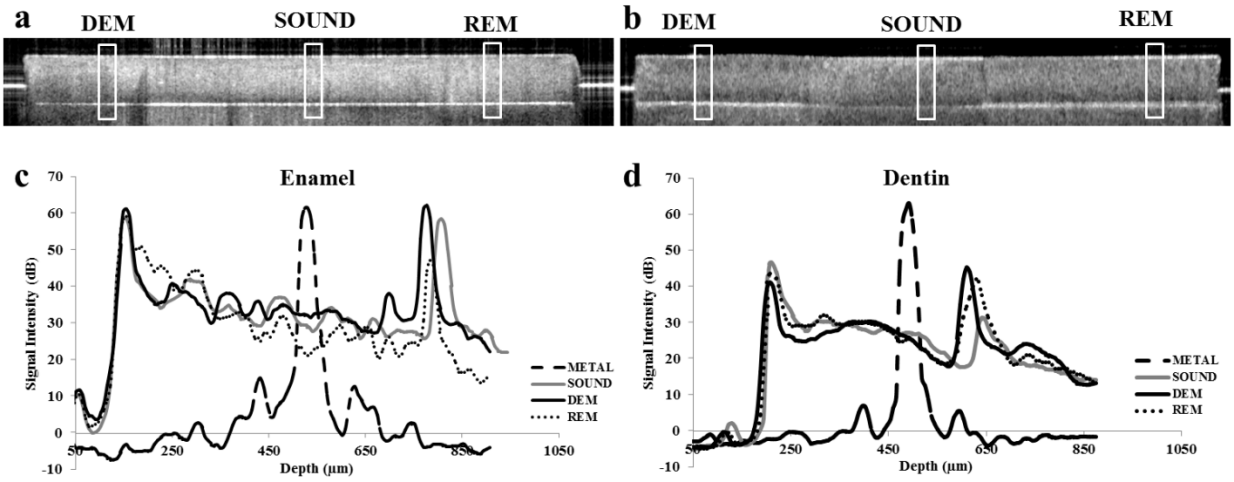

Figure. 2 (a-b) and (c-d) represent SS-OCT B-scan images of 40 and 80 depth levels of enamel and dentin specimens with corresponding A-scan signal intensity profiles after exposure to the de- and remineralized solutions, respectively. DEM= demineralized area, REM= remineralized area.

TMR analysis

After *n* measurement, the slices were subjected to TMR analysis to confirm the created lesion parameters and draw the MC-depth profiles. The enamel specimens were dehydrated in ascending alcohol solutions (25%-100%), embedded in epoxy resin to prevent chipping of the specimen edges, and further polished to obtain a uniform thickness of 120 µm using an automatic polishing machine (ML-160 A, Maruto, Tokyo, Japan).(97) Dentin slices were polished to reach 250-µm thickness without dehydration and embedding, and were soaked in 70% glycerol solution to prevent shrinkage of the specimens 15 min prior to

imaging. (54) TMR microradiographs of the polished specimens were captured and analyzed to draw MC-depth profiles over the 50-µm-wide central area using a custom setup previously described (54, 97) considering the maximum MC of the sound (non-treated) enamel and dentin to be 87 and 48 (vol.%), respectively. In order to establish point-by-point correlations between MC and *n*, mean MC was averaged over 17 µm depth (equivalent to the spot size of OCT laser beam) centered at each 20-µm or 40- µm depth in enamel and dentin.

Statistical analysis

Relationships between *n* and MC in demineralized and remineralized enamel and dentin were examined by Pearson's correlation. ANCOVA was used to compare linear regressions of *n* and MC between demineralized and remineralized zones in enamel or dentin. All the statistical procedures were performed at significant level of α=0.05 with the PASW Statistics package (Ver. 18 for windows; IBM, Armonk, New York, USA).

Results

Typical OCT B-scan images of enamel and dentin specimens at a certain depth from surface together with corresponding average signal intensity profiles after exposure to the de- and remineralized solutions, were shown in Fig. 2 (a-d). While the surface peaks of the three zones were found at the same optical depth coordinate, the bottom peaks were different due to variations in the OPLs after de/remineralization.

Figure 3 (a-d) showed average *n* and MC depth profiles through the regions in enamel and dentin. The profiles obtained by both methods in two substrates visually appeared to be similar in shape. The TMR results confirmed that all the specimens showed subsurface enamel and dentin lesions with depth of 137.4±11.04 and 329.1± 5.25 respectively.

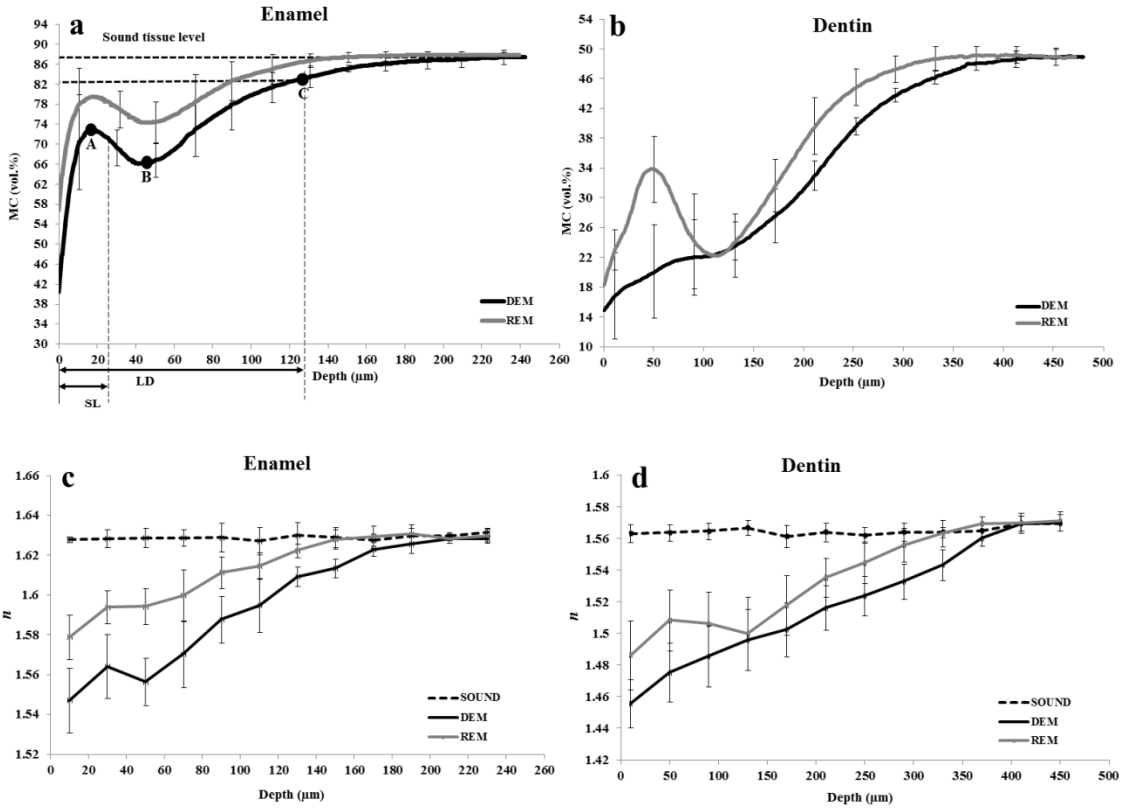

Figure. 3 The representative TMR mineral profiles (a-b) corresponded to the *n* vs. depth profiles (c-d) of enamel and dentin demineralized and remineralized specimens respectively. DEM= demineralized area, REM= remineralized area. In TMR mineral profile of a subsurface enamel lesion (b), A= Maximum MC, and B= Minimum MC. C= MC reaches 95% of sound tissue level (lesion depth, LD), SL= surface layer. Maximum MC at the sound enamel is 87 vol.%. Thickness of surface layer is defined as depth of a layer from surface to the depth where the MC is equal to the mean MC of Maximum and Minimum MC of the lesion body.

In Fig. 4, relationships between *n* and MC in enamel and dentin were shown. Pearson correlation found a significant ($p<0.001$) relationship between the variables (r=0.94, CI=0.92 to 0.96) and (r=0.93, CI=0.90 to 0.95) for demineralized and remineralized enamel and (r=0.93, CI=0.90 to 0.95) and (r=0.91, CI= 0.88 to 0.94) for demineralized and

remineralized dentin respectively. ANCOVA revealed that a significant difference ($p<0.01$) was found in the regression line slopes between remineralized and demineralized zones in enamel. In dentin, the intercepts were significantly different ($p < 0.01$), while the slopes were not ($p > 0.05$).

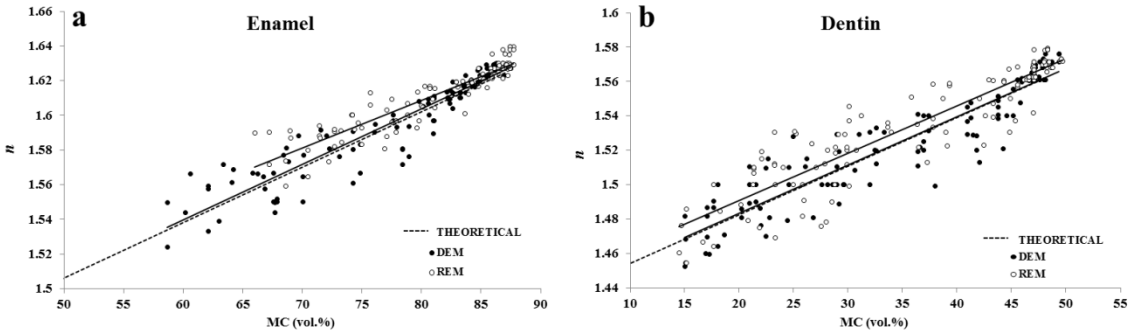

Figure. 4 (a) representing relationship between *n* and MC measurement for demineralized and remineralized enamel (y=0.32x+1.35, R^2=0.89 and y=0.28x+1.39, R^2=0.86) respectively. (b) Represent relationship between *n* and MC measurement for demineralized and remineralized dentin (y=0.28x+1.43, R^2=0.87, y=0.27x+1.44, R^2=0.84) respectively. Theoretical enamel (y=0.32x+1.35) and dentin (y=0.28x+1.43) derived from estimated values of components in Gladstone-Dale relation showed the same slope and intercept values as experimental results of demineralized enamel and dentin, respectively. DEM= demineralized area, REM= remineralized area.

Discussion

During demineralization, preferential dissolution of more acid-soluble phases of enamel (i.e. carbonate and magnesium-rich phases) causes an enlargement of the intercrystalline spaces, facilitating diffusion of acids through the microstructure. The porous structure with

lower MC and higher content of water may possess a smaller *n*.(98) The scatter plots in Fig. 4 (a, b) indicated a strong linear relationship between the two variables in both substrates, suggesting that the MC changes of the tissue could be estimated from local *n*. The parameters in the resulting linear equation are worth considering; the same MC in remineralized groups corresponded to higher *n* values compared to demineralized groups, particularly in enamel. In this regard, it has been suggested that in addition to MC, *n* of enamel depends on chemical composition of the crystallites.(85)

It is well known that biologically produced apatite is not pure hydroxyapatite (HAp); as it may contain and the other trace elements. (99) Remineralization of demineralized enamel and dentin proceeds through several stages, including formation and growth of new crystals and regrowth of preexisting crystals. Calcium and phosphate from remineralization solution diffuse into the tooth and with the help of fluoride, improve the crystallinity in terms of the purity, i.e., formation of fluoridated apatite with less carbonate and magnesium. (100) MC

determined from microradiography may not reveal information on the crystalline structure, (101) which depends on various factors such as solution DS with respect to each mineral and pH..

In order to clarify the differences between refractive indices of various forms of apatite, authors of the current study carried out additional experiments using contact fluids (Shimadzu Device Corporation, Nagano, Japan) with standard refractive indices and beck-line method (102) with synthetic apatite powders (Bio-Rad Laboratories, Tokyo, Japan) and bovine enamel powder. The following order was observed for *n*; fluoroapatite>pure HAp>bovine enamel powder>carbonated HAP (data not shown). It seems that the formation and replacement of a denser fluoridated apatite lattice with a higher *n* than that of the original carbonated apatite should be the main cause of higher *n* in remineralized group, and the difference in regression line slopes between demineralized and remineralized enamel. Further investigations are needed to reveal crystallographic information of enamel after remineralization. The relationship between *n* and volume

fraction (vol.%) of a particle of interest in a medium has been described by theoretical models. (103) The experimental results of the study were used to confirm a simple model (Gladstone–Dale) where the n_{total} of a mixture can be expressed as the partial sum of the refractive indices of its components, n_1, n_2, …, n_N, weighted by the volume fraction of each component, $f_1, f_2, \ldots, f_N$,:

$$n_{total} = n_1 f_1 + n_2 f_2 + ... + n_N f_N \qquad (1)$$

From the experimental regression, a completely demineralized enamel would have an n equal to the y-intercept (1.35); this value is slightly higher than n of water (1.33), and could be described by the presence of a small amount of proteins in the organic matrix of enamel. Applying the Eq. 1 for this substrate, with an estimated $n_{organic\ matrix}$=1.53, suggests $f_{organic\ matrix}$=8 vol.%, which is in the range of values reported for organic content of young bovine teeth. (104) These values are in turn applied for sound enamel in the equation, as a mixture of 87 vol.% of mineral crystals ($n_{mineral}$=1.65), (65) and the surrounding medium composed of organic matrix and water, resulting in the value of 1.62, which compares

with the values obtained in the study and those reported in the literature. (49, 90). The strong agreement between the theoretical and experimental regressions of *n* (Fig. 4a), supports the validity of the present experimental approach for studying the relation between *n* and MC in enamel.

It has been reported that unlike enamel, structural orientation of dentin could affect *n* of dentin tissue; (90) in the current study, a small variation in *n* was found for the sound bovine root dentin blocks. Similar to enamel which is mainly composed of apatite, a strong correlation between *n* and MC was found for this bio composite. Interestingly, in the completely demineralized dentin, the intercept of the linear regression (1.43) corresponds with the *n* of fully hydrated collagen (main organic component of dentin) experimentally measured in the near-IR region. (105, 106) This value falls exactly halfway between those of dry collagen (1.53) and water (1.33), confirming that collagen absorbs a quantity of water equivalent to its original volume when fully hydrated. (105, 106) The straightforward rule of density in *n* that worked

well in enamel can be extended to the dentin, assuming that the organic matrix volume fraction changed with increased water content as a result of demineralization, and that volume changes due to hydration occurred only in the interfibrilar space of collagen. (107)

The resulting *n* profiles through the lesion in the current study were in close association with those of MC; features such as maximum MC at surface zone, minimum MC in lesion body and sound tissue level on TMR profiles corresponded well with *n* profiles (Fig. 3). Therefore, the cross-sectional and simple measurement method introduced can be used to map *n* and provide interesting information on dental tissue *in vitro*, independent from OCT signal analysis methods known to date.

Measurement of *n* has important clinical implications too; decrease of *n* depends on the extent of demineralization, and conversely, *n* may serve as an indicator to diagnosis an monitor caries.(108) *In vivo* measurement of *n* by tracking the OCT focal length shift that results from translating the focus along the optic axis within the tissue has been documented.

Conclusion

In this study, an experimental approach was developed to measure the individual MC and the corresponding *n* at the different lesion depths in de- and remineralized enamel and dentin. The results indicated that the structure of caries could be determined with a good accuracy from local *n*.

Acknowledgements

This work was supported by the grant from the Global COE, at TMDU. The authors thank Drs. Aoki and Ohya for providing the X-ray source. The authors declare no conflicts of interest.

General Conclusions

Chapter 1 concluded that in etch-and- rinse adhesive system, the bond strength significantly decreased with aging in dentin. The results of nanoleakage evaluation implied that an increase has been detected in an earlier stage then when a significant drop was observed in bond strength, with the dentin bond being more susceptible to deterioration.

Chapter 2 concluded that SS-OCT is a useful tool for investigation of optical properties of human dental tissue and from which additional physical parameters such as *n* and OCTSS may be derived in addition to cross-sectional imaging. A prior knowledge of these features and their relations with the histology and pathology will provide verification of the diagnostic power of OCT.

Chapter 3 and 4 concluded that, an experimental approach was developed to measure the individual MC and the corresponding *n* at the different lesion depths in de- and remineralized enamel and dentin. The results indicated that the structure of caries could be determined with a good accuracy from local *n*.

The study in chapters 1 employed FE-SEM and micro-shear bond-strength test and silver staining technique; the results provided a qualitative and quantitative analysis of nanoleakage and evaluation of adhesive materials. It was also suggested that simple bond-strength tests are not the comprehensive methods to address and compare all the effective attributes of adhesive materials. Development of more sophisticated and clinically relevant laboratory techniques for standardized evaluation of adhesive materials will be a crucial progress in this regard.

In Chapters 2, 3 and 4 an OCT technique was used as an alternative approach for non-invasive characterization of dental hard tissue and caries. The method used in the mentioned chapters was not appropriate for *in vivo* studies and further experiments should be performed to develop hardware suitable for clinical measurement of local n in dental tissue as a diagnostic parameter.

References:

1. Buonocore MG. A simple method of increasing the adhesion of acrylic filling materials to enamel surfaces. *J Dent Res* 1955;34(6):849-53.

2. Burrow MF, Thomas D, Swain MV, Tyas MJ. Analysis of tensile bond strengths using Weibull statistics. *Biomaterials* 2004;25(20):5031-5.

3. Carvalho RM, Chersoni S, Frankenberger R, Pashley DH, Prati C, Tay FR. A challenge to the conventional wisdom that simultaneous etching and resin infiltration always occurs in self-etch adhesives. *Biomaterials* 2005;26(9):1035-42.

4. De Munck J, Van Meerbeek B, Yoshida Y, Inoue S, Vargas M, Suzuki K, et al. Four-year water degradation of total-etch adhesives bonded to dentin. *J Dent Res* 2003;82(2):136-40.

5. Fusayama T. Total etch technique and cavity isolation. *J Esthet Dent* 1992;4(4):105-9.

6. Pashley DH, Ciucchi B, Sano H, Horner JA. Permeability of dentin to adhesive agents. *Quintessence Int* 1993;24(9):618-31.

7. Van Meerbeek B, De Munck J, Yoshida Y, Inoue S, Vargas M, Vijay P, et al. Buonocore memorial lecture. Adhesion to enamel and dentin: current status and future challenges. *Oper Dent* 2003;28(3):215-35.

8. Watson TF, Pilecki P, Cook RJ, Azzopardi A, Paolinelis G, Banerjee A, et al. Operative dentistry and the abuse of dental hard tissues: confocal microscopical imaging of cutting. *Oper Dent* 2008;33(2):215-24.

9. Nakabayashi N, Kojima K, Masuhara E. The promotion of adhesion by the infiltration of monomers into tooth substrates. *J Biomed Mater Res* 1982;16(3):265-73.

10. Nakabayashi N, Nakamura M, Yasuda N. Hybrid layer as a dentin-bonding mechanism. *J Esthet Dent* 1991;3(4):133-8.

11. Gwinnett AJ. Moist versus dry dentin: its effect on shear bond strength. *Am J Dent* 1992;5(3):127-9.

12. Hashimoto M, Ohno H, Kaga M, Endo K, Sano H, Oguchi H. In vivo degradation of resin-dentin bonds in humans over 1 to 3 years. *J Dent Res* 2000;79(6):1385-91.

13. Li H, Burrow MF, Tyas MJ. The effect of thermocycling regimens on the nanoleakage of dentin bonding systems. *Dent Mater* 2002;18(3):189-96.

14. Miyazaki M, Sato M, Onose H. Durability of enamel bond strength of simplified bonding systems. *Oper Dent* 2000;25(2):75-80.

15. Reis AF, Arrais CA, Novaes PD, Carvalho RM, De Goes MF, Giannini M. Ultramorphological analysis of resin-dentin interfaces produced with water-based single-step and two-step adhesives: nanoleakage expression. *J Biomed Mater Res B Appl Biomater* 2004;71(1):90-8.

16. Sano H, Yoshiyama M, Ebisu S, Burrow MF, Takatsu T, Ciucchi B, et al. Comparative SEM and TEM observations of nanoleakage within the hybrid layer. *Oper Dent* 1995;20(4):160-7.

17. Sano H, Takatsu T, Ciucchi B, Horner JA, Matthews WG, Pashley DH. Nanoleakage: leakage within the hybrid layer. *Oper Dent* 1995;20(1):18-25.

18. Larson TD. The clinical significance and management of microleakage. Part two. *Northwest Dent* 2005;84(2):15-9.

19. Soderholm KJ. Correlation of in vivo and in vitro performance of adhesive restorative materials: a report of the ASC MD156 Task Group on Test Methods for the Adhesion of Restorative Materials. *Dent Mater* 1991;7(2):74-83.

20. Hashimoto M, Fujita S, Nagano F, Ohno H, Endo K. Ten-years degradation of resin-dentin bonds. *Eur J Oral Sci* 2010;118(4):404-10.

21. Okuda M, Pereira PN, Nakajima M, Tagami J. Relationship between nanoleakage and long-term durability of dentin bonds. *Oper Dent* 2001;26(5):482-90.

22. Yamazaki PC, Bedran-Russo AK, Pereira PN. The effect of load cycling on nanoleakage of deproteinized resin/dentin interfaces as a function of time. *Dent Mater* 2008;24(7):867-73.

23. Skovron L, Kogeo D, Gordillo LA, Meier MM, Gomes OM, Reis A, et al. Effects of immersion time and frequency of water exchange on durability of etch-and-rinse adhesive. *J Biomed Mater Res B Appl Biomater* 2010;95(2):339-46.

24. Stanislawczuk R, Reis A, Loguercio AD. A 2-year in vitro evaluation of a chlorhexidine-containing acid on the durability of resin-dentin interfaces. *J Dent* 2011;39(1):40-7.

25. Shimada Y, Tomimatsu N, Suzuki T, Uzzaman MA, Burrow MF, Tagami J. Shear bond strength of tooth-colored indirect restorations bonded to coronal and cervical enamel. *Oper Dent* 2005;30(4):468-73.

26. Tay FR, Pashley DH, Yoshiyama M. Two modes of nanoleakage expression in single-step adhesives. *J Dent Res* 2002;81(7):472-6.

27. Tiryakioglu M, Hudak D. Unbiased estimates of the Weibull parameters by the linear regression method. *J Mater Science* 2008;43(6):1914-19.

28. IOF S. Guidance on testing of adhesion to tooth structure. ISO TR 11450 Geneva switzerland: ISO ISO; 1994:1-14.

29. Gale MS, Darvell BW. Thermal cycling procedures for laboratory testing of dental restorations. *J Dent* 1999;27(2):89-99.

30. Tjandrawinata R, Irie M, Suzuki K. Twenty-four hour flexural and shear bond strengths of flowable light-cured composites: a comparison analysis using Weibull statistics. *Dent Mater J* 2007;26(4):589-97.

31. Shimada Y, Iwamoto N, Kawashima M, Burrow MF, Tagami J. Shear bond strength of current adhesive systems to enamel, dentin and dentin-enamel junction region. *Oper Dent* 2003;28(5):585-90.

32. Sadr A, Ghasemi A, Shimada Y, Tagami J. Effects of storage time and temperature on the properties of two self-etching systems. *J Dent* 2007;35(3):218-25.

33. Scherrer SS, Cesar PF, Swain MV. Direct comparison of the bond strength results of the different test methods: a critical literature review. *Dent Mater* 2010;26(2):e78-93.

34. Miyazaki M, Sato M, Onose H, Moore BK. Influence of thermal cycling on dentin bond strength of two-step bonding systems. *Am J Dent* 1998;11(3):118-22.

35. Helvatjoglu-Antoniades M, Koliniotou-Kubia E, Dionyssopoulos P. The effect of thermal cycling on the bovine dentine shear bond strength of current adhesive systems. *J Oral Rehabil* 2004;31(9):911-7.

36. Makishi P, Shimada Y, Sadr A, Wei S, Ichinose S, Tagami J. Nanoleakage Expression and Microshear Bond Strength in the Resin Cement/Dentin Interface. *J Adhes Dent* 2009.

37. Reis AF, Giannini M, Pereira PN. Long-term TEM analysis of the nanoleakage patterns in resin-dentin interfaces produced by different bonding strategies. *Dent Mater* 2007;23(9):1164-72.

38. Agee KL, Pashley EL, Itthagarun A, Sano H, Tay FR, Pashley DH. Submicron hiati in acid-etched dentin are artifacts of desiccation. *Dent Mater* 2003;19(1):60-8.

39. Malacarne J, Carvalho RM, de Goes MF, Svizero N, Pashley DH, Tay FR, et al. Water sorption/solubility of dental adhesive resins. *Dent Mater* 2006;22(10):973-80.

40. Lai SC, Tay FR, Cheung GS, Mak YF, Carvalho RM, Wei SH, et al. Reversal of compromised bonding in bleached enamel. *J Dent Res* 2002;81(7):477-81.

41. Shimada Y, Tagami J. Effects of regional enamel and prism orientation on resin bonding. *Oper Dent* 2003;28(1):20-7.

42. Hashimoto M, Tay FR, Ohno H, Sano H, Kaga M, Yiu C, et al. SEM and TEM analysis of water degradation of human dentinal collagen. *J Biomed Mater Res B Appl Biomater* 2003;66(1):287-98.

43. Reis A, Loguercio AD. A 36-month clinical evaluation of ethanol/water and acetone-based etch-and-rinse adhesives in non-carious cervical lesions. *Oper Dent* 2009;34(4):384-91.

44. Wojtkowski M. High-speed optical coherence tomography: basics and applications. *Appl Opt* 2010;49(16):D30-61.

45. Chen Y, Otis L, Piao D, Zhu Q. Characterization of dentin, enamel, and carious lesions by a polarization-sensitive optical coherence tomography system. *Appl Opt* 2005;44(11):2041-8.

46. Amaechi BT, Higham SM, Podoleanu AG, Rogers JA, Jackson DA. Use of optical coherence tomography for assessment of dental caries: quantitative procedure. *J Oral Rehabil* 2001;28(12):1092-3.

47. Baumgartner A, Dichtl S, Hitzenberger CK, Sattmann H, Robl B, Moritz A, et al. Polarization-sensitive optical coherence tomography of dental structures. *Caries Res* 2000;34(1):59-69.

48. Huang D, Swanson EA, Lin CP, Schuman JS, Stinson WG, Chang W, et al. Optical coherence tomography. *Science* 1991;254(5035):1178-81.

49. Meng Z, Yao XS, Yao H, Liang Y, Liu T, Li Y, et al. Measurement of the refractive index of human teeth by optical coherence tomography. *J Biomed Opt* 2009;14(3):034010.

50. Colston BW, Jr., Everett MJ, Da Silva LB, Otis LL, Stroeve P, Nathel H. Imaging of hard- and soft-tissue structure in the oral cavity by optical coherence tomography. *Appl Opt* 1998;37(16):3582-5.

51. Choma M, Sarunic M, Yang C, Izatt J. Sensitivity advantage of swept source and Fourier domain optical coherence tomography. *Opt Express* 2003;11(18):2183-9.

52. Ishibashi K, Ozawa N, Tagami J, Sumi Y. Swept-source optical coherence tomography as a new tool to evaluate defects of resin-based composite restorations. *J Dent* 2011;39(8):543-8.

53. Shimada Y, Sadr A, Burrow MF, Tagami J, Ozawa N, Sumi Y. Validation of swept-source optical coherence tomography (SS-OCT) for the diagnosis of occlusal caries. *J Dent* 2010;38(8):655-65.

54. Natsume Y, Nakashima S, Sadr A, Shimada Y, Tagami J, Sumi Y. Estimation of lesion progress in artificial root caries by swept source optical coherence tomography in comparison to transverse microradiography. *J Biomed Opt* 2011;16(7):071408.

55. Bakhsh TA, Sadr A, Shimada Y, Tagami J, Sumi Y. Non-invasive quantification of resin-dentin interfacial gaps using optical coherence tomography: validation against confocal microscopy. *Dent Mater* 2011;27(9):915-25.

56. Makishi P, Shimada Y, Sadr A, Tagami J, Sumi Y. Non-destructive 3D imaging of composite restorations using optical coherence tomography: marginal adaptation of self-etch adhesives. *J Dent* 2011;39(4):316-25.

57. Girija V, Stephen HCY. Characterization of lipid in mature enamel using confocal laser scanning microscopy. *J Dent* 2003;31(5):303-11.

58. Fernandes CP, Chevitarese O. The orientation and direction of rods in dental enamel. *J Prosthet Dent* 1991;65(6):793-800.

59. Lynch CD, O'Sullivan VR, McGillycuddy CT, Dockery P, Rees JS, Sloan AJ. Hunter–Schreger Bands and their implications for clinical dentistry *J Oral Rehabil* 2011;38:359-65.

60. Lynch CD, O'Sullivan VR, Dockery P, McGillycuddy CT, Sloan AJ, Anatomy Jo. Hunter-Schreger Band patterns in human tooth enamel. *J Anat* 2010;217:106-15.

61. Osborn JW. A 3-dimensional model to describe the relation between prism directions, parazones and diazones, and the Hunter-Schreger bands in human tooth enamel. *Arch Oral Biol* 1990;35(11):869-78.

62. Wang XJ, Milner TE, de Boer JF, Zhang Y, Pashley DH, Nelson JS. Characterization of dentin and enamel by use of optical coherence tomography. *Appl Opt* 1999;38(10):2092-6.

63. Zijp JR, Bosch JJ. Theoretical model for the scattering of light by dentin and comparison with measurements. *Appl Opt* 1993;32(4):411-5.

64. Fried D, Glena RE, Featherstone JDB, Seka W. Nature of lightscattering in dental enamel and dentin at visible and nearinfrared wavelengths. *Appl Opt* 1995;34:1278-85.

65. Zijp JR, ten Bosch JJ, Groenhuis RA. HeNe-laser light scattering by human dental enamel. *J Dent Res* 1995;74(12):1891-8.

66. Shimamura Y, Murayama R, Kurokawa H, Miyazaki M, Mihata Y, Kmaguchi S. Influence of tooth-surface hydration conditions on optical coherence-tomography imaging. *J Dent* 2011;39(8):572-77.

67. Knuttel A, Bonev S, Knaak W. New method for evaluation of in vivo scattering and refractive index properties obtained with optical coherence tomography. *J Biomed Opt* 2004;9(2):265-73.

68. Wang X, Zhang C, Zhang L, Xue L, Tian J. Simultaneous refractive index and thickness measurements of bio tissue by optical coherence tomography. *J Biomed Opt* 2002;7(4):628-32.

69. Uhlhorn SR, Borja D, Manns F, Parel JM. Refractive index measurement of the isolated crystalline lens using optical coherence tomography. *Vision Res* 2008;48(27):2732-8.

70. Tearney GJ, Brezinski ME, Southern JF, Bouma BE, Hee MR, Fujimoto JG. Determination of the refractive index of highly scattering human tissue by optical coherence tomography. *Opt Lett* 1995;20(21):2258-60.

71. Guo X, Guo Z, Wei H, Yang H, He Y, Xie S, et al. In vivo comparison of the optical clearing efficacy of optical clearing agents in human skin by quantifying permeability using optical coherence tomography. *Photochem Photobiol* 2011;87(3):734-40.

72. Larin KV, Motamedi M, Ashitkov TV, Esenaliev RO. Specificity of noninvasive blood glucose sensing using optical coherence tomography technique: a pilot study. *Phys Med Biol* 2003;48(10):1371-90.

73. Darling CL, Huynh GD, Fried D. Light scattering properties of natural and artificially demineralized dental enamel at 1310 nm. *J Biomed Opt* 2006;11(3):34023.

74. Zolotarev VM, Grisimov VN. Architectonics and optical properties of dentin and dental enamel. *Opt and Spectros* 2001;90(5):753-59.

75. Tsuda H, Arends J. Orientational micro-Raman spectroscopy on hydroxyapatite single crystals and human enamel crystallites. *J Dent Res* 1994;73(11):1703-10.

76. Trunina NA, Lychagov VV, Tuchin VV. Study of water diffusion in human dentin by optical coherent tomography. *Opt and Spectros* 2010;109(2):162-68.

77. Kienle A, Michels R, Hibst R. Magnification--a new look at a long-known optical property of dentin. *J Dent Res* 2006;85(10):955-9.

78. Walton RE, Outhwaite WC, Pashley DF. Magnification--an interesting optical property of dentin. *J Dent Res* 1976;55(4):639-42.

79. Zolotarev VM, Tulin DV, Oreshkov AB, Volchek BZ, Drichko NM, Kolpakova NV. Interference of light in composite systems of ordered anisotropic fibers. Part 2. Optical study of how the structural organization of dentine tubules affects the structure and shape of the crown of the tooth. *J Opt Technol* 2002;69(3):146-50.

80. Senawongse P, Otsuki M, Tagami J, Mjor IA. Morphological characterization and permeability of attrited human dentine. *Arch Oral Biol* 2008;53(1):14-9.

81. Marshall GW, Jr., Marshall SJ, Kinney JH, Balooch M. The dentin substrate: structure and properties related to bonding. *J Dent* 1997;25(6):441-58.

82. Ohmi M, Ohnishi Y, Yoden K, Haruna M. In vitro simultaneous measurement of refractive index and thickness of biological tissue by the low coherence interferometry. *IEEE Trans Biomed Eng* 2000;47(9):1266-70.

83. Okada H, Sadr A, Shimada Y, Tagami J. Micro-shear bond strength of current one-step adhesives to cementum and dentin. *Am J Dent* 2009;22(5):259-63.

84. Tagami J, Tao L, Pashley DH. Correlation among dentin depth, permeability, and bond strength of adhesive resins. *Dent Mater* 1990;6(1):45-50.

85. Besic FC, Wiemann MR, Jr. Dispersion staining, dispersion, refractive indices in early enamel caries. *J Dent Res* 1972;51(4):973-85.

86. Houwink B. The index of refraction of dental enamel apatite. *Br Dent J* 1974;137(12):472-5.

87. Sadr A, Mayoral Molina J, Shimada Y, Bakhsh TA, Cho E, Tagami J. Real-time Tomographic Monitoring of Composite Restoration Placement Using SS-OCT. *J D Res* 2010;89(Spec Iss A.):1501.

88. Fried D, Xie J, Shafi S, Featherstone JD, Breunig TM, Le C. Imaging caries lesions and lesion progression with polarization sensitive optical coherence tomography. *J Biomed Opt* 2002;7(4):618-27.

89. Sadr A, Shimada Y, Mayoral Molina J, Hariri I, Bakhsh TA, Sumi Y, et al. Swept source optical coherence tomography for quantitativeand qualitative assessment of dental composite restorations. *ProcSPIE* 2011;7884:78840C.

90. Hariri I, Sadr A, Shimada Y, Tagami J, Sumi Y. Effects of structural orientation of enamel and dentine on light attenuation and local refractive index: An optical coherence tomography study. *J Dent* 2012;40(5):387-96.

91. Featherstone JD. Dental caries: a dynamic disease process. *Aust Dent J* 2008;53(3):286-91.

92. Jones RS, Fried D. Remineralization of enamel caries can decrease optical reflectivity. *J Dent Res* 2006;85(9):804-08.

93. Jones RS, Darling CL, Featherstone JDB, Fried D. Imaging artificial caries on the occlusal surfaces with polarization-sensitive optical coherence tomography. *Caries Res* 2006;40(2):81-89.

94. Manly RS, Hodge HC, Ange LE. Density and Refractive Index Studies of Dental Hard Tissues : II. Density Distribution Curves 1,2. *J D Res* 1939;18:487-95.

95. Wiemann MRJR, Besic FC, Keller O. Application of dispersion staining to the study of refractive index of dental enamel. *J Dent Res* 1970;49(1):174.

96. Kidd EA, Fejerskov O. What constitutes dental caries? Histopathology of carious enamel and dentin related to the action of cariogenic biofilms. *J Dent Res* 2004;83 .(Spec No C):C35-38.

97. Hamba H, Nikaido T, Sadr A, Nakashima S, Tagami J. Enamel Lesion Parameter Correlations between Polychromatic Micro-CT and TMR. *J Dent Res* 2012.

98. Nazari A, Sadr A, Campillo-Funollet M, Nakashima S, Shimada Y, Tagami J, et al. Effect of hydration on assessment of early enamel lesion using swept-source optical coherence tomography. *J Biophotonics* 2012.

99. LeGeros RZ, Sakae T, Bautista C, Retino M, LeGeros JP. Magnesium and carbonate in enamel and synthetic apatites. *Adv Dent Res* 1996;10(2):225-31.

100. Phantumvanit P, Feagin FF, Koulourides T. Strong and weak acid sampling for fluoride of enamel remineralized in sodium fluoride solutions. *Caries Res* 1977;11(1):52-61.

101. Kitasako Y, Sadr A, Hamba H, Ikeda M, Tagami J. Gum Containing Calcium Fluoride Reinforces Enamel Subsurface Lesions in situ. *J Dent Res* 2012;91(4):370-5.

102. Deetlefs M, Seddon KR, Shara M. Neoteric optical media for refractive index determination of gems and minerals. *New J Chem* 2006;30(3):317-26.

103. Emslie AG, Aronson JR. Spectral reflectance and emittance of particulate materials. 1: theory. *Appl Opt* 1973;12(11):2563-72.

104. Robinson C, Kirkham J, Hallsworth AS. Volume distribution and concentration of protein, mineral and water in developing bovine enamel. *Arch Oral Biol* 1988;33(3):159-62.

105. Wang XJ, Milner TE, Chang MC, Nelson JS. Group refractive index measurement of dry and hydrated type I collagen films using optical low-coherence reflectometry. *J Biomed Opt* 1996;1(2):212-6.

106. Bashkatov AN, Genina EA, Kochubey VI, Tuchin VV. Estimation of wavelength dependence of refractive index of collagen fibers of scieral tissue. *Proc SPIE* 2000;4162:265-8.

107. Kim YL, Walsh JT, Jr., Goldstick TK, Glucksberg MR. Variation of corneal refractive index with hydration. *Phys Med Biol* 2004;49(5):859-68.

108. Churchley D, Lynch RJ, Lippert F, Eder JS, Alton J, Gonzalez-Cabezas C. Terahertz pulsed imaging study to assess remineralization of artificial caries lesions. *J Biomed Opt* 2011;16(2):026001.